Rotation Periods of the Hyades Open Cluster using ASAS Light Curves: Measuring the Hyades Gyro-Age and Benchmarking Tools for Gyrochronology Studies with LSST

Alisha Kundert

Adviser:
Phillip Cargile

Thesis Committee:
Paul Sheldon
Keivan Stassun
David Weintraub

Abstract. Rotation period distributions for older open clusters are difficult to obtain because of the general scarcity of clusters with ages greater than 200 Myr, as well as the challenge of measuring rotation periods for less active older stars. This has clouded our knowledge of how stars spin down as they evolve from the zero-age main sequence. A key piece of our understanding of how stellar rotation rates change over time relies on the study of the nearby ($\sim$45 pc) and old ($\sim$625 Myr) Hyades open cluster. We present the results from a detailed analysis of the rotation period distribution of the Hyades in an effort to estimate the gyro-age of this benchmark open cluster. Analyzing All Sky Automated Survey (ASAS) light curves with 14+ year baselines, we measure rotation periods for Hyades members by applying a period-finding technique that combines the Lomb-Scargle periodogram and Monte Carlo simulations to optimize period detection in long-baseline, low-cadence light curves that potentially suffer from time-dependent changes, e.g. star spot evolution. We derive 67 rotation periods for Hyades members, 40 of which are determined for the first time. These rotation periods measured from ASAS light curves allow us to characterize the rotation period distribution of the Hyades, enabling the application of current gyrochronology models to calculate a rotation-age for the cluster. Additionally, using ASAS data provides a valuable test of our ability to determine rotation periods in future low-cadence, extended duration surveys, such as the Large Synoptic Survey Telescope (LSST).

1. Introduction

Stellar rotation must be taken into account when determining the structure and fundamental parameters of stars (e.g., Meynet and Maeder 1997). Therefore, understanding the angular momentum evolution of stars is critical to formulating the full picture of stellar evolution. Through the comparison of the angular momentum distribution of open clusters of different ages, it has been determined that stars lose angular momentum as they age (Skumanich 1972). The decrease of stellar rotation over time is attributed to the stellar wind, a constant outflow of charged particles spewed from the atmposphere of a star (Parker 1958; Weber and Davis 1967; Schatzman 1962). The strength of the stellar wind is regulated by the stellar magnetic field that is generated by a dynamo maintained by rotation (Mestel and Spruit 1987). The feedback between the stellar magnetic field and angular momentum causes stars of a similar mass and age to have a similar rotation period (Kawaler 1988). This forms the foundation of gyrochronology, an empirically based relation between stellar age, mass, and rotation (Barnes 2003). Gyrochronology is a powerful method for determining stellar ages because it only requires a rotation period and a mass to determine an age for a star. This makes it practical to determine the ages of individual stars, which is otherwise exceptionally difficult or impossible for other chronometers (Barnes 2007).

The empirical and theoretical models that underpin gyrochronology require testing and calibration using stellar populations with well determined ages. Open clusters provide a key resource for constraining gyrochronology due to their large populations of coeval stars with ages determined using other chronometers. However, the scarcity of old open clusters has left gyrochronology relatively poorly constrained at ages greater than ~ 200 Myr. The Hyades, being an older ($\sim$625 Myr) open cluster, therefore provides a powerful benchmark for stellar rotation.

Gyrochronology has the potential to be a fruitful application of data from the Large Synoptic Telescope (LSST). The LSST is in the process of being built on Cerro Pachõn in northern Chile and is expected to begin releasing data in 2021. The LSST will survey the entire available night sky every three nights in multiple wavelength bands with high precision. With its ability to go wide and deep (3 degree field-of-view and down to r$\sim$27 mag), it will amass large amounts of data on many faint celestial objects (LSST Science Collaborations et al. 2009). The LSST will measure light curves for a great number of stars in open clusters, thus providing the ability to improve the fitting of gyrochronology models to the cluster rotation sequences. Most valuably, gyrochronology methods could determine ages of field stars that will constitute a large portion of the stars imaged by the LSST. Determining ages from measured rotation periods for millions of stars in the LSST database will allow us to assemble a stellar formation map of a significant portion of the Milky Way.

One major challenge of applying gyrochronology to LSST data is that the LSST is expected to only generate 200-300 data points for a given star over a span of 10 years. Such a small number of data points over a long duration of time makes it difficult to detect rotation periods because starspot evolution and stellar cycles have a significant effect on the magnitude modulation of long baseline light curves. To test whether rotation periods can be measured from this type of data we have conducted a rotation period study of the Hyades using All Sky Automated Survey (ASAS) data that is of a similar cadence and baseline to what is projected for the LSST. We derive new rotation periods for cluster members, adding to the literature rotation distribution of the Hyades (Radick et al. 1987; Delorme et al. 2011).

We describe the ASAS light curves used in our study in Section 2. In Section 3 we explain how we have determined Hyades cluster membership. Our methods of measuring Hyades rotation periods are outlined in Section 4 and the results of this analysis are shown in Section 5. The application of gyrochronology models to our results is described in Section 6 and the potential for determining rotation periods from LSST data is discussed in Section 7.

2.   ASAS Data for the Hyades

For our study of Hyades rotation periods, we analyze publicly available photometric light curve data from ASAS (Pojmanski 2002). ASAS has a southern hemisphere observation station at Las Campanas Observatory in Chile that has collecting data since 1997, and a northern hemisphere station at Haleakala, Maui in operation since 2006. The goal of this survey is to continuously observe the entire available night sky to catalog sources of variable brightness, especially variable stars. ASAS observes with standard Johnson-Cousins V and I filters and has a photometric V band range between 7 - 14 magnitudes. We conducted our analysis using only the V magnitude observations.

ASAS provides photometric data taken simultaneously from five apertures that vary in pixel size. The smallest aperture is 2 pixels in diameter and is best suited to sources fainter than a V mag of 12. The largest aperture is 6 pixels in diameter and is best suited for sources brighter than a V mag of 9. The apertures in between the smallest and largest aperture cover the range between 9 - 12 mag. In our analysis, we have used the photometry from the aperture appropriate to the magnitude of each star in our sample. Additionally, ASAS provides a grade (A - D) for each observation, indicating the quality of that data. We have used only the data from observations with the best quality (grade A). A typical ASAS light curve for a star in the Hyades region extends for 14 years with an average of 250 grade A observations.

The average amplitude of variability present in our data is approximately .11 mag. To ensure that our expected minimum variability is detected above the magnitude dependent predicted RMS scatter for ASAS data, we have set a 2σ (RMS $\sim$0.06 mag) faintness limit of 12.25 mag (Fig. 1).

3.   Hyades Cluster Membership

Our sample of cluster members for the Hyades came from a number of sources. The majority of our cluster members were taken from previous Hyades studies (Radick et al. 1987; Delorme et al. 2011; Perryman et al. 1998). Perryman et al. based their cluster membership determination on Hipparcos astrometry (parallax and proper motion) and radial velocities. The Hipparcos data has since been re-reduced (van Leeuwen 2007) and this new data has altered the membership determination results made by the Perryman et al. study. For this reason, we performed additional membership cuts on the literature members.

Fundamentally, members of an open cluster lie on a distinct locus on a color magnitude diagram (CMD) because they are of the same age, distance, and metallicity (de Bruijne et al.
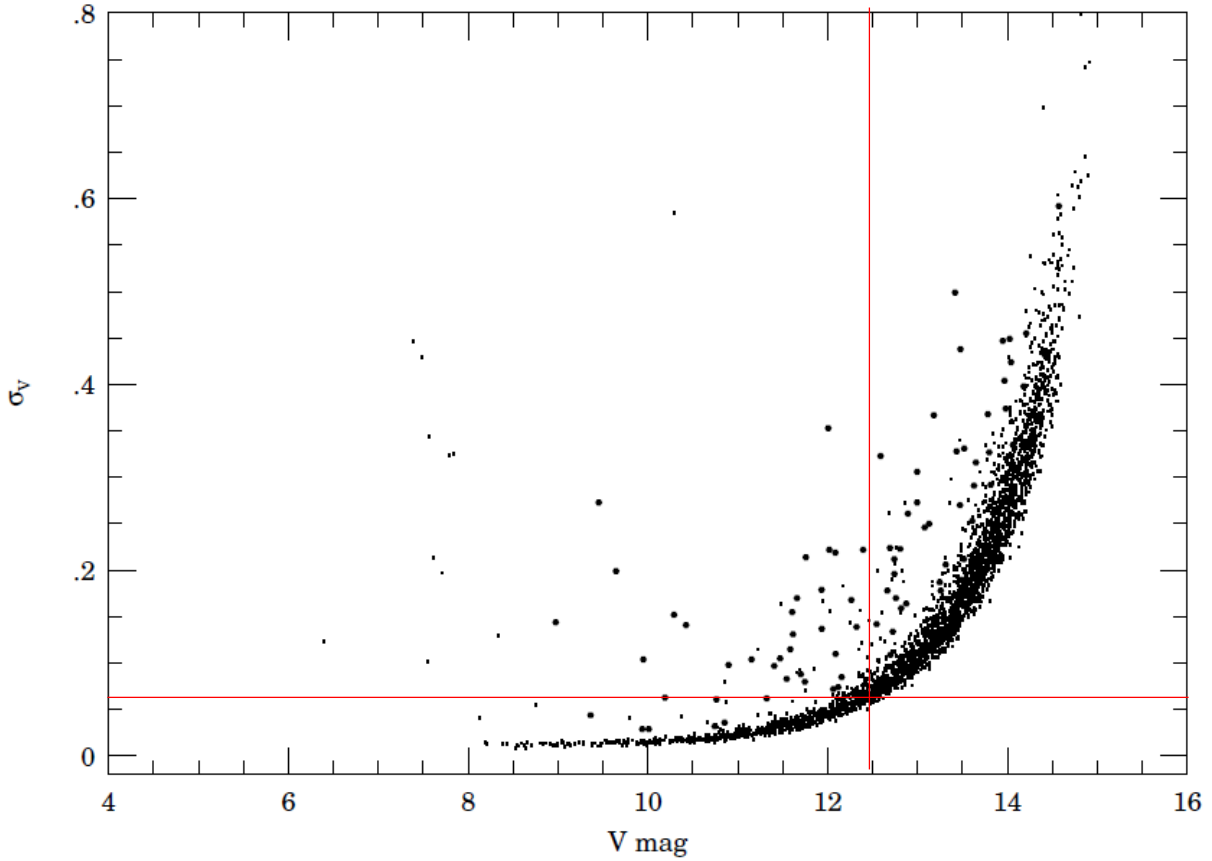
Fig. 1.— The precision of ASAS observations is dependent on the magnitude of the source being observed. Reliable rotation periods should be derived from σ_V values at less than half of the amplitude of variability (indicated by the horizontal line). This corresponds to magnitudes brighter than ~12.25 mag (indicated by the vertical line). This figure was adapted from Pojmanski (2002).

2001). The Hyades is known to have a tight cluster sequence for a visible CMD (van Leeuwen 2009), and we assume that because of this there will also be a clean sequence in the infrared. We assemble optical B and V photometry from the re-reduced Hipparcos data. If a star from the Radick et al. or Delorme et al. catalogs is not in the Hipparcos catalog, we use the literature B and V photometry. We additionally collect infrared J, H, K photometry from 2MASS. We have removed stars with measured rotation periods that fall half a magnitude below or a magnitude and a half above the cluster sequence. Fig. 2 shows the visible and infrared CMDs. Sources that met our membership criteria and had a measured rotation period are plotted in color. Grey data points are stars that were ultimately not used in this study. Those indicated by a ○ have no measured rotation period. Stars that we measured rotation periods for, but did not meet our membership criteria are marked with a x.

For our collection of stars with derived rotation periods, we additionally performed a 3σ cut on parallax as shown in Fig. 3. Using the new re-reduced data from Hipparcos, van Leeuwen determined the average parallax for Hyades cluster members to be ~21.53 mas (van Leeuwen 2009). The calculated mode for our Hyades parallax distribution is 21.72 mas, matching well with the value van Leeuwen calculated.

A study of Hyades membership using the re-reduced data was more recently conducted by employing a cone search around the cluster center (van Leeuwen 2009). This study was able to find cluster members missed using the old Hipparcos data, but unfortunately, this list of revised cluster members was not published. We carried out a cone search of the re-reduced data using similar parameters as those found in the van Leeuwen study to include the newly added cluster members to our sample. We searched the Hipparcos database for stars in a radius of 13 degrees centered on the Hyades cluster center (RA = 66.73 degrees, DEC = 15.87 degrees) with parallax of 22 ± 10 mas and Hp > 7 mag.

The majority of stars found in our search were already in the previous literature studies, but we were able to find a few new potential members. After assembling our list of potential cluster members, we looked at the CMD to remove nonmembers based on their position above and below the sequence in the same way that was conducted for the literature members. ASAS data was then collected for the list of new cone search members.

4.   Light Curve Analysis Methodology

4.1.   Sectioning the Light Curve

A star is classified as rotationally variable if the star's brightness changes over time due to rotation. The changes in magnitude of this type of star are due to starspots, long-term
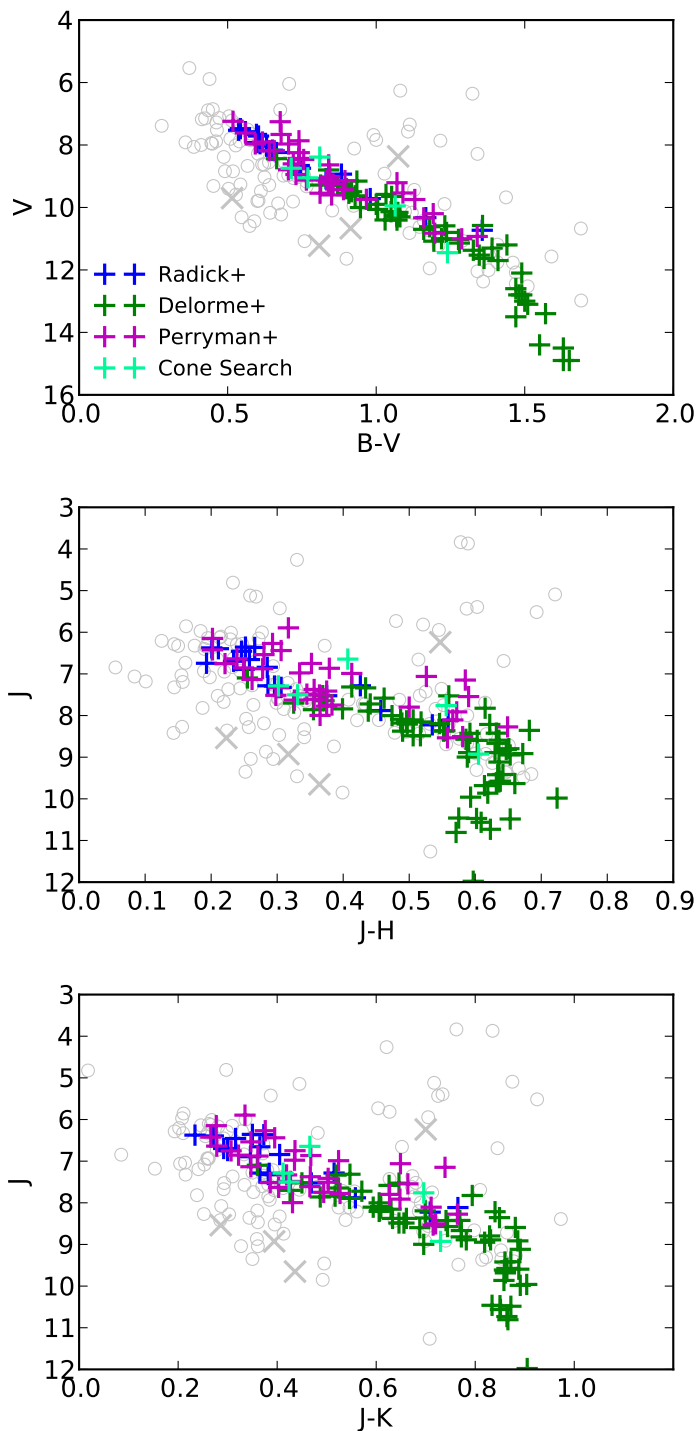
Fig. 2.— Color-magnitude diagrams for our cluster sample. + data points are those stars with measured rotation periods that meet our membership cuts. Stars that did not meet our membership cuts or stars that do not have a measured rotation period are plotted in grey.
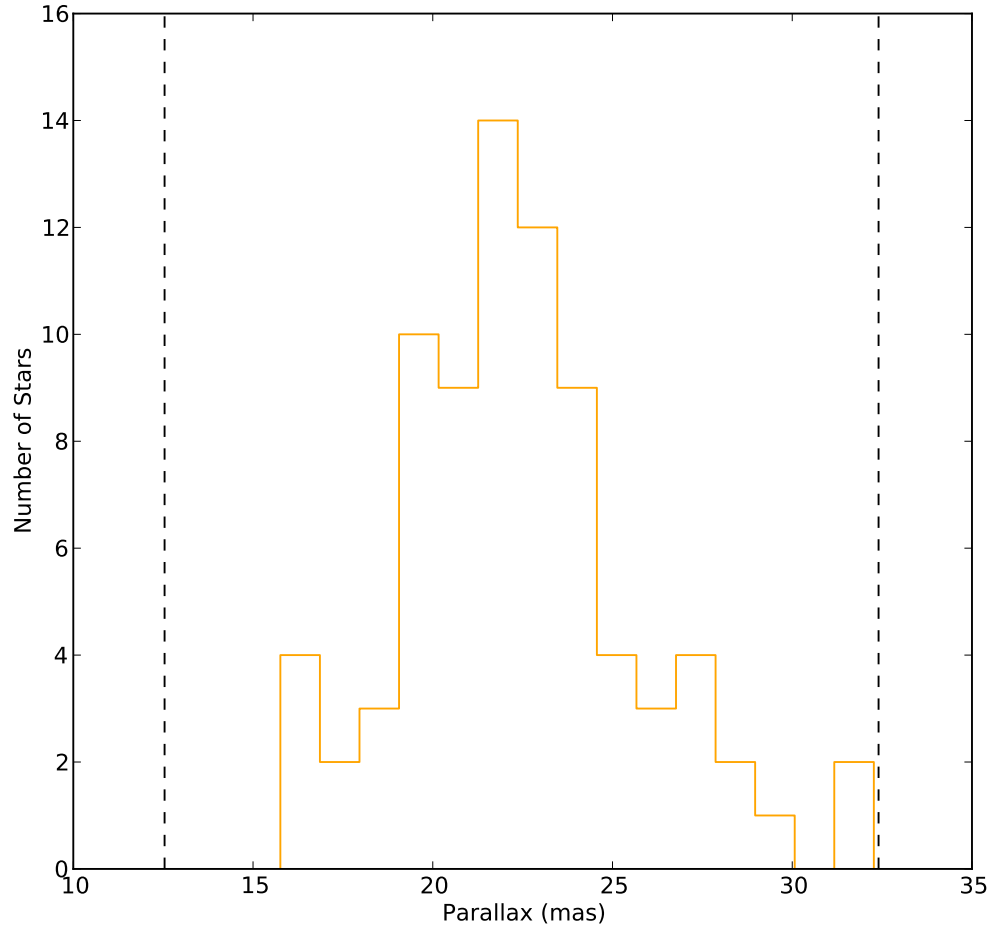
Fig. 3.— The parallax distribution of our cluster sample. The dashed lines indicate the 3σ boundaries from the mode of the distribution. There were no stars in our sample with parallaxes outside these limits.

surface features that appear as a result of the star's magnetic activity. Starspots are cooler than the surface that surrounds them and because of this, the magnitude of the star will diminish as they pass in front of the star (with respect to the observer), and begin to increase again as they pass behind the star. This results in a periodic variability of the brightness relating to the rotation of the star. The period of this variability, and thus the period of rotation, can be calculated using photometric observations.

Starspots typically form and then disappear in only a few months. If the duration of monitoring a star is longer than the lifetime of its starspots, the observed magnitude modulation will vary over the course of the observations. This is because changes in the number and size of the starspots effect the amplitude of the variability. Additionally, the phase of the periodic modulation will change as a result of starspots appearing and disappearing at different locations on the stellar surface (Messina et al. 2010). This makes it difficult to determine the rotation period over long time spans because many starspot cycles will be observed. It is especially difficult if, like ASAS, the light curves are sparsely sampled with a long baseline.

Sectioning the light curve into smaller windows of time, of a similar duration to the lifespan of a starspot, reduces the effect of starspot cycles and facilitates the determination of a star's rotation period in long duration data (e.g., Messina et al. 2010). Although the observed starspots may be different in each window, producing varying amplitudes and phases, the period of variability should stay the same because the rotation period of the star will have remained constant across the span of observations.

We applied two methods of dividing up our 14+ year ASAS light curves: static and dynamic sectioning. Static sectioning divides the light curve into windows with equal numbers of points. We found that seven was the optimal number of windows such that the number of points in each window was maximized while the time baseline of the window was minimized for the typical ASAS cadence. Dynamic sectioning divides the light curve into windows based on seasons of observation. We define a dynamic window as a set of at minimum 15 data points that do not contain a break of more than 60 days between consecutive time measurements. The time baseline of these windows is typically smaller than for the static windows. In Fig. 4, we show an example of an ASAS light curve with both static and dynamic windows displayed.
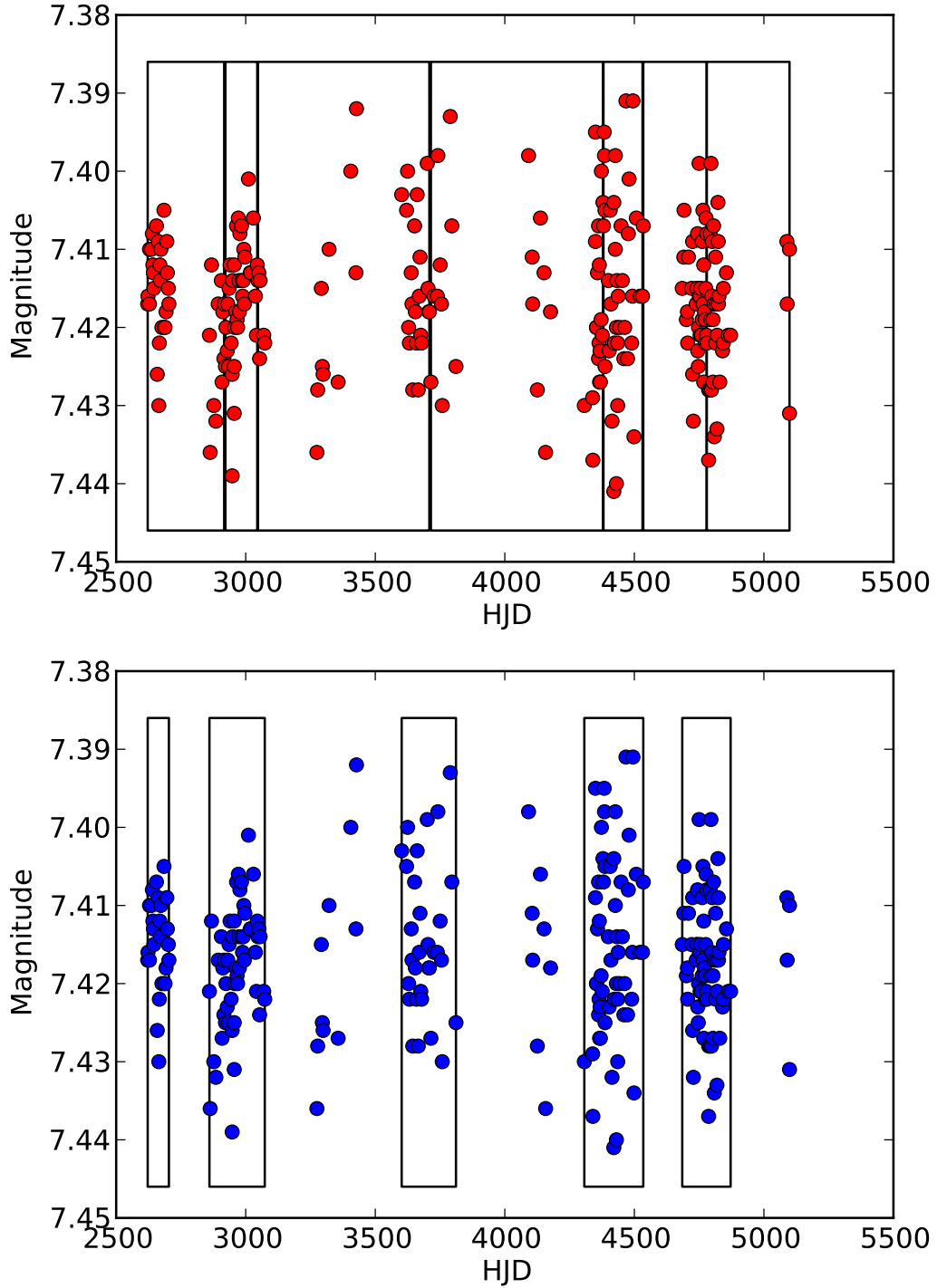
Fig. 4.— *Top*: static sectioning. *Bottom*: dynamic sectioning. The black lines indicate the edges of the windows. In the case of dynamic sectioning, any data point outside the black lines was not included in the final dynamic rotation period analysis.

4.2.   Periodograms and Coadding Power Spectra

After separately applying the two sectioning methods to a light curve, we used the Press and Rybicki (1989) Lomb-Scargle periodogram algorithm to identify and measure periodic signals for each window. The Lomb-Scargle periodogram is especially effective at determining periods of variability in unevenly sampled data like the ASAS light curves we are using. Calculating a periodogram involves fitting sinusoidal waves with a range of frequencies to the light curve data. For each wave of a given frequency that is applied to the data, a power is calculated. The power is a quantity based on the quality of fit between the model sine wave and the data. The frequency with the highest power is the frequency of the sinusoidal wave that best fits the data.

For a given frequency, the power at that frequency within multiple power spectra can be added together to create a new coadded power spectrum. Coadding increases the power of significant signals found in the constituent power spectra, while minimizing the power of random noise. For example, a frequency that has a large power in every power spectra that is coadded together will have a large peak in the resulting coadded power spectrum. Likewise, a frequency that has a weak power in every power spectra will have a small peak in the coadded power spectrum. Coadding enables the determination of the most significant frequencies contained within multiple power spectra. Fig. 5 shows an example of coadding the power spectra derived for the windows of a sectioned light curve.

When dealing with noisy power spectra, it is useful to calculate the joint power statistic (JPS) instead of the combined power (Sturrock et al. 2005). Because this method involves multiplying the powers at a specific frequency together instead of just adding them, calculating the JPS increases the height of significant peaks and decreases the noise level even more dramatically than just adding the powers together.

Sturrock et al. provides an algorithm to calcuate the JPS. The approximation equations for coadding n number of power spectra can be written in terms of X where $X = (S_1 \cdot S_2 \cdot ... \cdot S_n)^{\frac{1}{n}}$ and S_n is the power at a specific frequency in the nth power spectrum. The second through fifth order JPS approximation equations are found in the literature (Sturrock et al. 2005; Sturrock 2008) and are written here as Equations 1 through 4.

$$J_{2A} = \frac{1.943X^2}{0.650 + X} \tag{1}$$

$$J_{3A} = \frac{2.916X^2}{1.022 + X} \tag{2}$$

$$J_{4A} = \frac{3.881X^2}{1.269 + X} \tag{3}$$

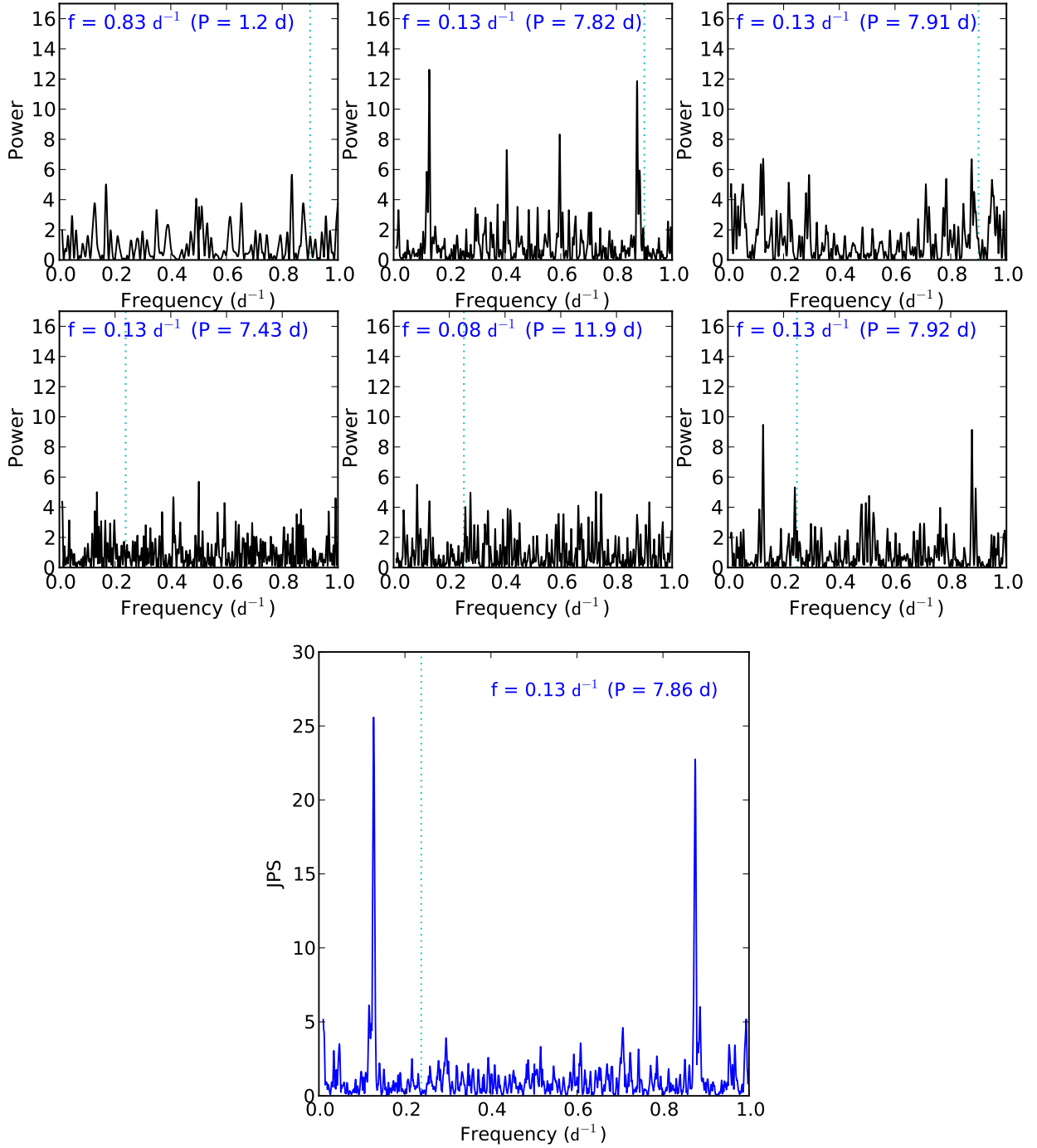Fig. 5.— *Top*: the Lomb-Scargle periodograms derived for 6 dynamic windows that the light curve was sectioned into. *Bottom*: The coadded power spectrum. When the window power spectra are coadded together, this power spectrum is the result. Coadding reveals that the strongest signal across all of the windows is at f = 0.13 d^{-1} for this star. The dotted line indicates the Nyquist frequency as discussed in Section 4.4.

$$J_{5A} = \frac{4.9X^2}{1.6 + X} \tag{4}$$

As part of our light curve analysis we coadd up to seven power spectra together. This made it necessary for us to derive the sixth and seventh order approximation equations, as these equations are not found in the literature. We determnie J_{6A} and J_{7A} following the derivation process outlined in Sturrock et al. (2005).

Sturock et al. found that:

$$J_n(X) = -\ln[C_{J,n}(X)] \tag{5}$$

where

$$C_{J,n+1}(X) = \int_0^\infty dx\, e^{-x}\, C_{J,n}\left(\frac{X^n}{x}\right). \tag{6}$$

Beginning with

$$C_{J,3}(X) = \int_0^\infty da\, e^{-a}\, 2\frac{X^{\frac{3}{2}}}{a^{\frac{1}{2}}} K_1\left[\frac{2X^{\frac{3}{2}}}{a^{\frac{1}{2}}}\right], \tag{7}$$

where K_1 is the first order modified Bessel function of the second kind, we derived the following equations:

$$C_{J,6}(X) = \int\int\int\int_0^\infty e^{-a-b-c-d}\frac{X^3}{(abcd)^{\frac{1}{2}}} K_1\left[\frac{2X^3}{(abcd)^{\frac{1}{2}}}\right] da\, db\, dc\, dd \tag{8}$$

$$C_{J,7}(X) = \int\int\int\int\int_0^\infty e^{-a-b-c-d-e}\frac{X^{\frac{7}{2}}}{(abcde)^{\frac{1}{2}}} K_1\left[\frac{2X^{\frac{7}{2}}}{(abcde)^{\frac{1}{2}}}\right] da\, db\, dc\, dd\, de\,. \tag{9}$$

Eq. 8 and Eq. 9 were numerically integrated over the range $X = 0.01$ to 40 with a step size of 0.01 for Eq. 8 and a step size of 1 for Eq. 9. The length of time required to numerically solve Eq. 9 did not allow for a smaller step size to be used. The results were plugged into Eq. 5 creating an array of J and corresponding X values. These calculated data points are shown in Fig. 6. This data was fit to an equation of the form $J_{nA} = \frac{AX^2}{B+X}$, which was found to be the most effective approximation equation form (Sturrock et al. 2005). We then determined:

$$J_{6A} = \frac{5.967X^2}{1.866 + X} \tag{10}$$
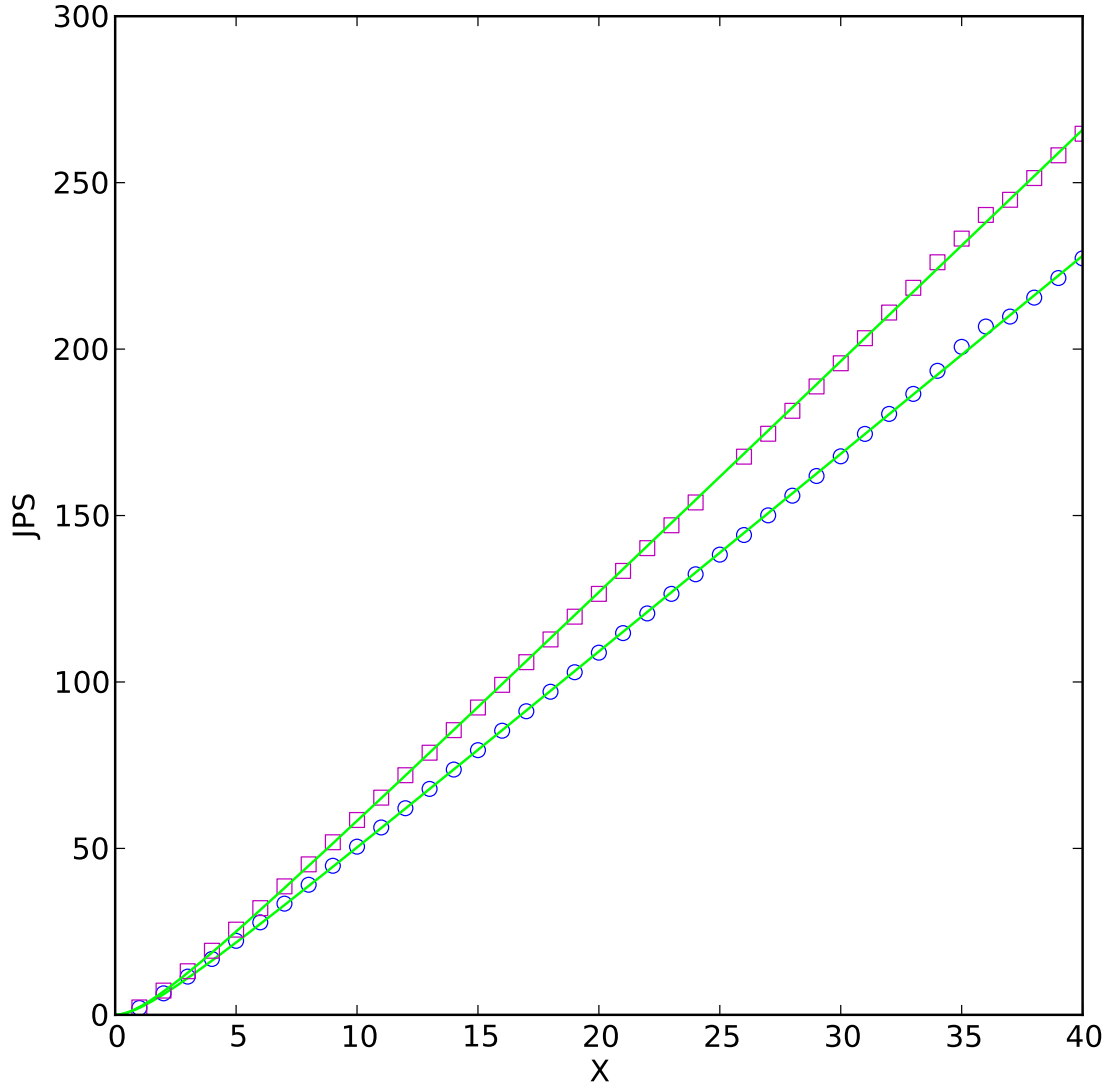
$$J_{7A} = \frac{6.975X^2}{1.972 + X} \tag{11}$$

Fig. 6.— The sixth (○) and seventh (□) order solutions to Eq. 5. The estimated values from J_{6A} and J_{7A} are indicated by the solid lines.

With J_{6A} and J_{7A} defined, we were able to coadd our sets of static and dynamic power spectra created from Hyades ASAS light curves.

4.3. Alias and Beat Frequency Detection

Alias peaks appear in our power spectra because of the periodic sampling rate of observation. Alias peaks form from the sampling rate beating with the period of the variability within the data. To identify the alias peaks within our power spectra, we derived a spectral window function for every static and dynamic window of the light curve. False alias peaks can be detected by introducing artificial variability into the data with the same observation epochs as the original light curve (Scargle 1982). This new data is then substituted for the magnitude measurements of the original data when the periodogram is calculated. Any peaks that appear in the new periodogram are alias or beat frequency peaks (not including the peak corresponding to the input frequency).

For every spectral window function calculated, we saw clear aliases at frequencies of 1 d^{-1} – the artificial frequency. This allowed us to reject peaks at frequencies of 1 d^{-1} - the rotational frequency in the real power spectra. These alias peaks are also present in the coadded power spectra, but because we have identified these false frequency values in the individual spectral window functions, we are able to reject them in the final light curve analysis.

Fig. 7 shows an example of alias detection from the spectral window function.

4.4. The Range of our Period Search

We looked for rotation periods between 1.1 and 40 days (corresponding to frequencies between 0.025 - 0.9 d^{-1}).

The maximum period for which we could reliably detect a signal from a window of data was restricted to the size of the window. Most windows were of a duration longer than 40 days, however, we set the maximum to 40 days as it is exceptionally unlikely that a solar-type star would have a period greater than this at an age of 625 Myr.

The minimum period we could reliably detect was determined by the Nyquist frequency. The Nyquist frequency ν_{Nyquist} is the minimum sampling frequency necessary to accurately fit a sinusoidal wave to variable data. A sampling frequency greater than ν_{Nyquist} allows for multiple sinusoids of different frequencies to fit the data equally well. For evenly sampled
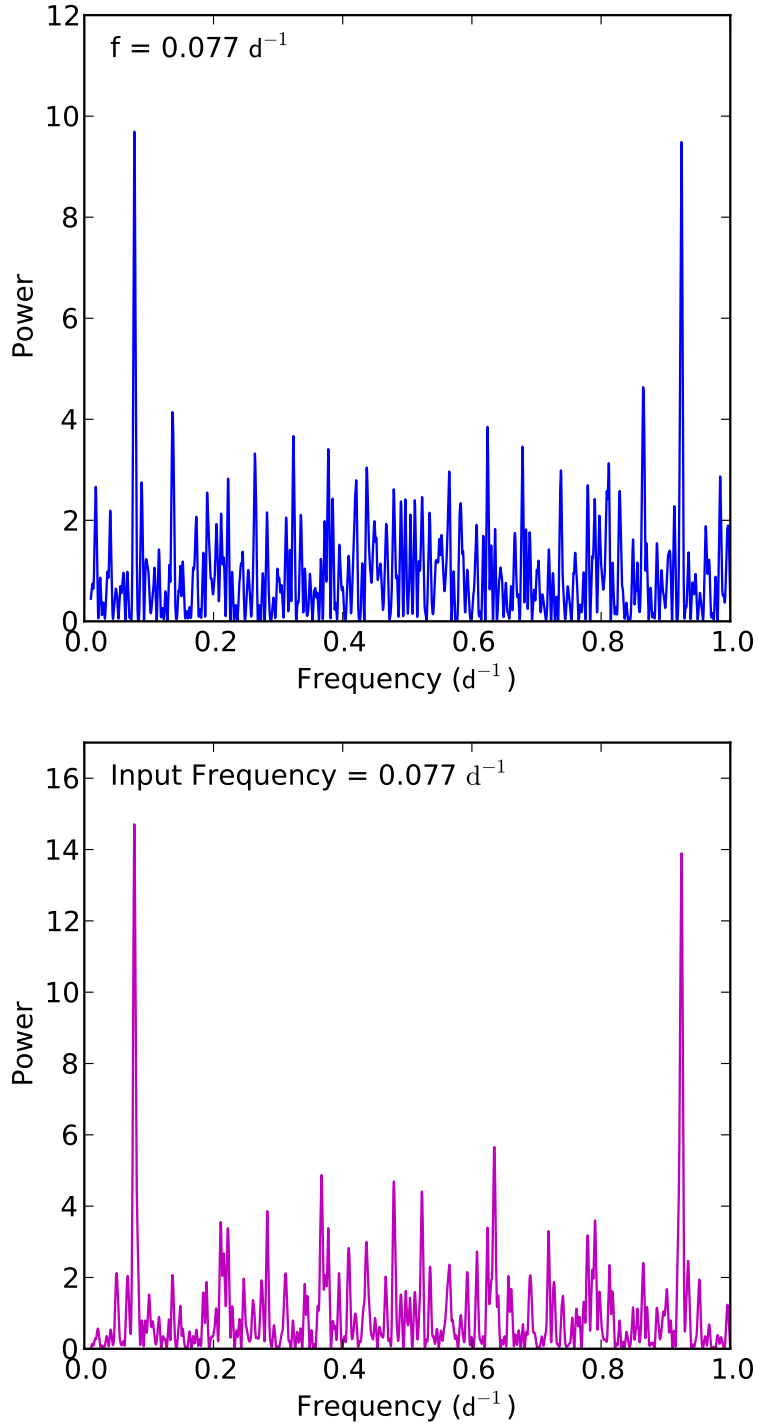
Fig. 7.— *Top*: The power spectrum derived for one window of original light curve data. *Bottom*: The spectral window function calculated from artificial data with a sinusoidal variability of the same frequency as the variability found in the original data. The alias peak at 1 - 0.077 d^{-1} originates from the periodic nature of the sampling times.

data, $\nu_{\text{Nyquist}} = \frac{1}{2\Delta}$ where Δ is the sampling interval. For unevenly spaced data, such as ASAS light curves, the Nyquist frequency has been determined by Roberts et al. (1987) to be:

$$\nu_{\text{Nyquist}} = \frac{1}{2\Delta_{min}} \tag{12}$$

where Δ_{min} is the minimum sampling interval over the span of data being analyzed. The average Nyquist frequency of the windows of our cluster sample was $\sim 0.5 \text{d}^{-1}$ (~ 2 d). We set an upper limit on the maximum frequency of our analysis to be 0.9 d^{-1}, as a result of aliasing around 1 day.

Fig. 5 shows an example of using the Nyquist frequency as a maximal frequency limit. Our period search algorithm looked for peaks within the range of frequencies smaller than ν_{Nyquist}. However, we note that the maximum frequency of any coadded power spectrum is determined by the minimum upper frequency bound of the constituent power spectra. This resulted in an average maximum frequency limit of $\sim 0.25 \text{ d}^{-1}$ (~ 4 d). Because of the aliasing discussed in Section 4.3, we verified that that a significant peak at frequency f found within the frequency range of our search had a greater power than the related $1 - f$ peak.

4.5. Statistical Tests for Significance

4.5.1. False Alarm Probability Analysis

The false alarm probability (FAP) is the probability that a spurious peak of a given power will be found in a light curve periodogram (Horne and Baliunas 1986). A power with a low FAP suggests it is improbable that a random peak at this power will be found; therefore, an identified peak at this height is unlikely to have arisen from random noise.

The most accurate method of determining the FAP for our window power spectra is through the use of Monte Carlo simulations (e.g., Herbst et al. 2002). For each window, the magnitude measurements for that data were randomly scrambled while the time values remained in place. The Lomb-Scargle periodogram was derived for this new scrambled data and the power of the greatest peak was recorded. This process was repeated for a total of 1000 times and a cumulative distribution function (CDF) was derived from the recorded results. The FAP of the greatest peak for each window was calculated by matching the corresponding power value on the CDF to the probability level on the CDF. The FAP is then equivalent to 1 - probability value.

An example of calculating the FAP for individual power spectra using Monte Carlo trials is shown in Fig. 8. This calculation allows us to isolate those windows with significant

peaks and coadd them together which can create a more reliable coadded power spectrum than what would result from coadding all of the window power spectra together as shown in Fig. 9.

The FAP for peaks in our coadded power spectra cannot be calculated through Monte Carlo simulations because they are created not directly created from the data - a coadded power spectrum is formed from previously derived power spectra. We instead calculate the FAP of the most significant peaks in our coadded power spectra using the equation:

$$\text{FAP} = 1 - (1 - e^{-S_P^*})^M \tag{13}$$

where

$$S_P^* \approx S_P - 1, \tag{14}$$

S_P is the power of the greatest peak, and M is the number of independent frequencies (Sturrock and Scargle 2010). We have assumed that M corresponds to the number of local maxima in our power spectra.

4.5.2. Determining the Probability of the Null Hypothesis

The null hypothesis is the probability that no variability is present in the time series. Testing for the null hypothesis provides an even more rigorous test than determining the significance of a peak based on the FAP. We use the formulation of Sturrock and Scargle (2010) to determine the probability of the null hypothesis $P(H_0)$ given by:

$$P(H_0) = \frac{\Omega(H_0)}{1 + \Omega(H_0)} \tag{15}$$

where

$$\Omega(H_0) = 2.44(1.92 + S_{EQ})e^{-S_{EQ}}, \tag{16}$$

$$S_{EQ} = -\log(1 - (1 - e^{-S_P^*})^M), \tag{17}$$

and S_P^* is given by Eq. 14. In our final light curve analysis we have calculated $P(H_0)$ for all of our coadded power spectra.
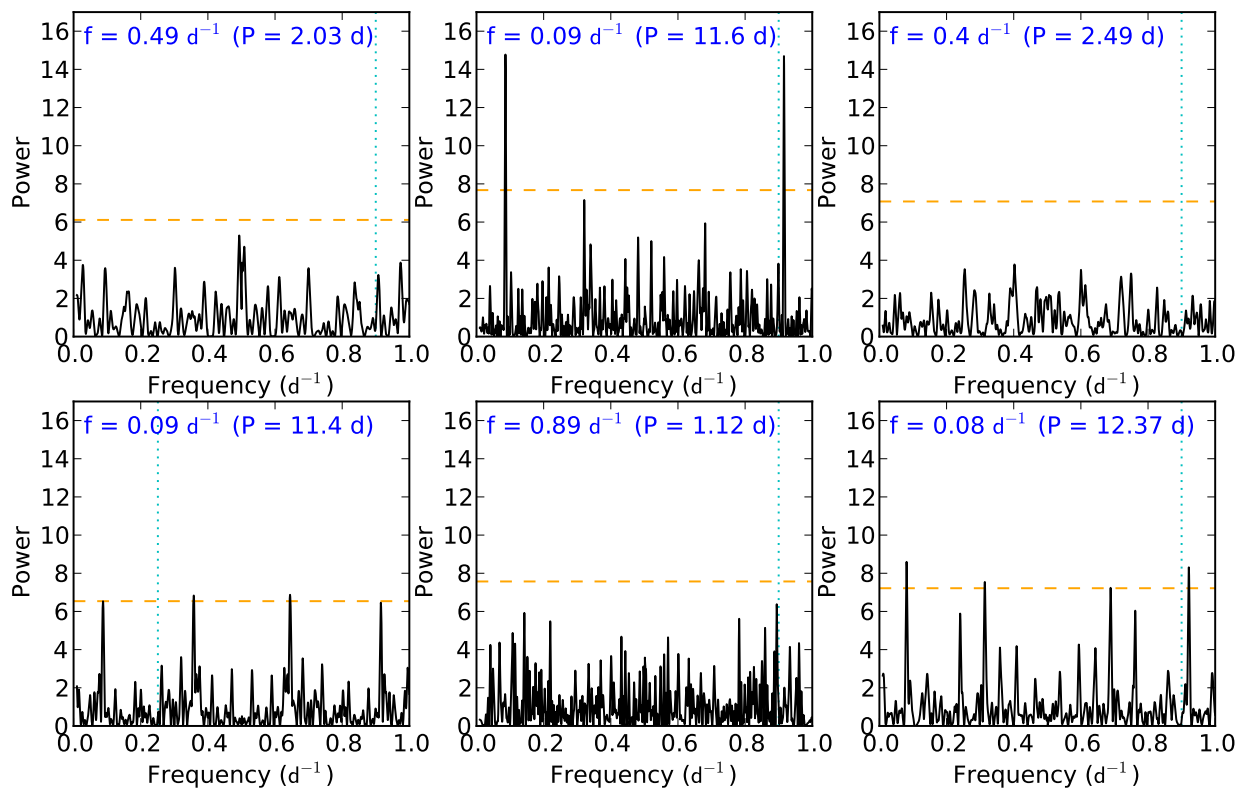
Fig. 8.— The Lomb-Scargle periodograms derived for a light curve sectioned into 6 dynamic windows. The horizontal dashed line indicates the .95 CDF confidence level as calculated from Monte Carlo trials. The peaks greater than this level are statistically significant. The vertical dashed line is the Nyquist frequency. The resulting coadded power spectra are shown in Fig. 9.
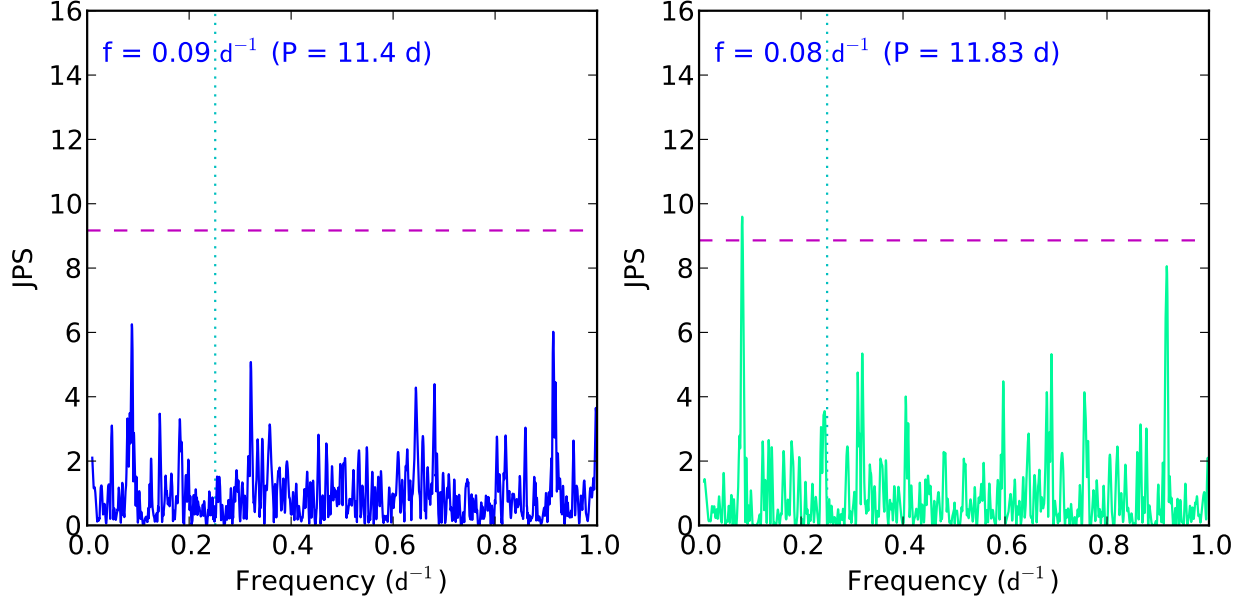
Fig. 9.— *Left*: the combined coadded power spectrum - the result of coadding all 6 power spectra from Fig. 8. *Right*: the selective coadded power spectrum - the result of coadding only those windows with a peak above the .95 CDF confidence level from Fig. 8 and within a frequency range with $\nu_{Nyquist}$ as the upper frequency bound. The dashed line indicates the .95 confidence level as calculated using Eq. 13. Peaks above this level have a FAP of less than .05 and are statistically significant. Because the selective coadded power spectrum is created from only those power spectra with statistically strong peaks, it often has fewer significant peaks and a tallest peak with a greater JPS than the combined coadded power spectrum. The vertical dashed line in both power spectra is the Nyquist frequency.

4.6.   Putting in all together: determination of final rotation periods

The final determination of the rotation period for a Hyades member involves a synthesis of the methods discussed previously. For a given light curve, a static coadded power spectrum was created by coadding the seven static windows together, and a dynamic coadded power spectrum was created by coadding the dynamic windows together. It was apparent that for some stars, one sectioning method was more effective than the other at returning a period. Independently applied, each sectioning method returned approximately the same number of periods; however, rotation periods were not found for all of the same stars.

For example, using our final method we derived periods for a total of 27 stars in the Radick et al. and Delorme et al. catalogs. Originally, for 6 of the 27 stars, the correct period would be derived for one sectioning method but not the other. However, when the static and dynamic coadded power spectra were coadded together, the resulting combined coadded power spectrum returned the correct period for those 6 of the sample that previously disagreed in addition to another 4 stars that previously had undetermined periods. Additionally, the combined coadded power spectrum had significant peaks with a greater signal-to-noise and less spurious peaks. The effectiveness of creating the combined coadded power spectrum is shown in Fig. 10.

Furthermore, for each sectioning method, we coadded each window of that method that had a peak greater than the .95 level on the CDF to create a selective coadded power spectrum. We coadded the static selective and dynamic selective coadded power spectrum to create the combined selective coadded power spectrum which was useful to compare to the combined coadded power spectrum when a star had a noiser light curve. This process is shown and described in Fig. 8 and Fig. 9.

A periodogram was also derived when no sectioning was used. It returned the correct period for approximately 12/27 of the stars with previously determined periods that we were able to match.

The combined coadded power spectrum, the combined selective coadded power spectrum, and the no windows power spectrum were the three main power spectra we looked at for determining rotation periods. The FAP was calculated using Eq. 13 for these three power spectra within the appropriate period search range as described by Section 4.4. The probability of the null hypothesis was additionally calculated for each of the coadded power spectra using Eq. 15. It was found that $P(H_0)$ offered a considerably more conservative test of statistical significance than the FAP. Restricting our final designation of reliability to peaks with a $P(H_0) < .05$ enabled the greatest accuracy when matching periods found in the literature.
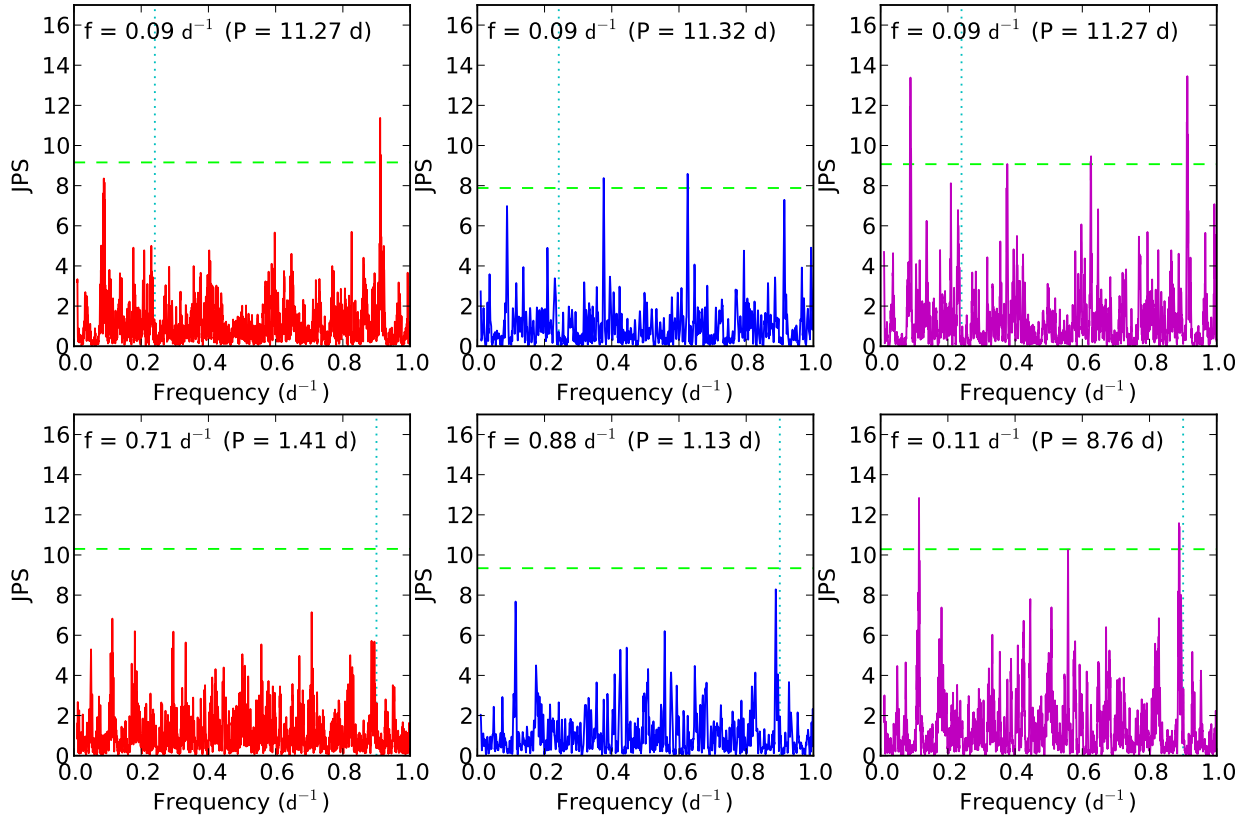
Fig. 10.— *Top Row*: the static (red), dynamic (blue), and combined coadded (purple) power spectra for ASAS ID 043951+1243.7. For this star, the static sectioning method is more effective at turning out the rotation period. *Bottom Row*: the static, dynamic, and combined coadded power spectra for ASAS ID 043035+1544.0. For this star, the dynamic sectioning method is more effective. Both of these examples show how the combined coadding of the static and dynamic coadded power spectra allows for the best determination of the rotation period.

If there were more than one peak with a $P(H_0)$ less than 5% and the periods corresponding to these peaks were greater than 1 day apart (Section 5.1), the light curves were phased to the periods. After visual inspection, the period that phased the data best was selected, if there was not a significant difference in the order of the phased light curves, the period for that star was considered to be undetermined. Otherwise, if the star has passed through all the criteria in our analysis, we concluded the derived rotation period to be reliable. Our newly derived rotation periods and the literature periods can be found listed in Tables 1 and 2.

5. Results

We measured rotation periods for a total of 67 Hyades open cluster members; 40 of these rotation periods are determined for the first time. Of the 40 newly determined periods, 31 are for single stars and 9 are for stars flagged as binaries in the literature. We have combined our period measurements and the period determinations of Radick et al. and Delorme et al. into a table of single stars (Table 1) and binary stars (Table 2). The contribution of our newly determined periods to the overall sample of Hyads with determined periods is shown in period space (Fig. 11) and B-V space (Fig. 12).

Table 1:: Period distribution for single stars in the Hyades. P indicates our period measurement. If applicable, P_{lit} is the period determined by the literature source in the reference column. LC PTS refers to the number of datapoints within the ASAS light curve for that star. The note column indicates whether our determined period matches the literature, or whether our period is newly determined from the Perryman et al. catalog or cone search. References - R: Radick et al. (1987), D: Delorme et al. (2011), PE: Perryman et al. (1998), C: our cone search as described in Section 3.

ASAS ID	HIP ID	P (d)	P_{lit} (d)	V (mag)	B-V (mag)	J (mag)	H (mag)	K (mag)	plx (mas)	LC Pts	note	Ref.
031733+0741.4	15310	8.8000	-	7.9043	0.617	6.639	6.4	6.361	23.95	190	P = new	PE
032029+0827.3	15563	10.9700	-	9.7449	1.13	7.545	6.955	6.881	32.05	197	P = new	PE
033030+2006.2	16329	7.0200	-	8.429	0.739	6.977	6.643	6.542	25.26	324	P = new	PE
033250+2341.5	16529	9.3400	-	9.0249	0.844	7.374	7.018	6.907	22.81	213	P = new	PE
034347+2051.7	-	-	12.3	-	9	10.484	9.831	9.612	-	59	-	D
034812+0708.8	17766	12.3900	-	10.9282	1.34	8.273	7.624	7.509	26.8	238	P = new	PE
035025+1714.8	17962	11.4200	-	9.5995	0.85	7.776	7.401	7.249	22.69	235	P = new	PE
035103+2354.2	18018	8.3700	-	10.3326	1.16	8.106	7.54	7.395	28.27	217	P = new	PE
035234+1115.6	-	-	13.29	-	1.54	9.864	9.245	9.006	-	139	-	D
035453+1618.9	-	-	6.04	-	1.58	9.96	9.367	9.056	-	56	-	D
035501+1229.1	18322	-	11.66	10.2666	1.07	8.181	7.692	7.574	25.62	309	-	D
035506+1659.9	18327	9.7500	-	9.1429	0.895	7.413	7.038	6.91	23.86	272	P = new	PE
040339+1927.3	18946	-	11.45	10.2487	1.07	8.206	7.709	7.6	23.27	248	-	D
040526+1926.5	19082	-	13.51	11.5264	1.347	8.889	8.259	8.107	15.76	218	-	D
040540+1756.2	19098	9.0800	-	9.43	0.89	7.748	7.365	7.254	18.54	240	P = new	PE
040616+1541.9	19148	7.4100	-	7.9661	0.593	6.753	6.532	6.446	21.77	206	P = new	PE
040635+1333.0	-	-	16.68	13.5	1.47	9.982	9.258	9.091	-	174	-	D
040701+1520.1	19207	-	11.98	10.6168	1.18	8.365	7.811	7.665	24.19	208	-	D
040743+1631.1	19263	11.5200	12.3	10.0621	1.005	8.105	7.599	7.511	19.67	229	P = P_{lit}	D
040811+1652.4	-	32.6900	13.63	11.1	1.44	8.766	8.106	7.933	-	231	P $\neq$ P_{lit}	D
040827+1211.5	19316	-	12.96	11.3704	1.327	8.818	8.171	8.046	25.93	255	-	D
040836+2346.1	-	-	9.35	9.4	0.9	7.84	7.441	7.323	-	192	-	D

Table 1 – continued from previous page

ASAS ID	HIP ID	P (d)	P_{lit} (d)	V (mag)	B-V (mag)	J (mag)	H (mag)	K (mag)	plx (mas)	LC Pts	note	Ref.
040949+0918.3	19441	12.5200	-	10.1989	1.192	7.912	7.34	7.264	32.27	202	P = new	PE
041014+1722.1	19472	4.7100	-	9.208	1.07	7.061	6.535	6.412	26.98	228	P = new	PE
041022+1204.7	19481	20.8800	-	8.2461	0.741	6.749	6.397	6.313	23.92	231	P = new	PE
041128+1559.4	-	-	1.79	14.9	1.65	10.807	10.236	9.941	-	3	-	D
041427+1226.1	19786	6.1000	-	8.1813	0.64	6.856	6.607	6.534	23.29	296	P = new	PE
041431+2334.3	19793	8.3400	-	8.1839	0.657	6.877	6.599	6.516	21.08	187	P = new	PE
041510+1423.9	19834	-	13.91	11.6311	1.363	8.947	8.294	8.128	27.31	214	-	D
041633+2154.4	19934	-	10.26	9.2823	0.813	7.701	7.376	7.275	19.07	183	-	D
041725+1901.8	-	-	12.95	11	1.22	8.597	7.994	7.909	-	267	-	D
041728+1454.2	-	-	2.35	14.4	1.55	10.471	9.869	9.621	-	50	-	D
041728+2328.1	20012	8.4800	-	11.4476	1.24	8.926	8.321	8.196	27.63	187	P = new	C
041819+1605.6	20082	-	12.64	9.7157	0.98	7.88	7.423	7.322	18.9	209	-	R
041858+1954.4	20130	-	9.39	8.7442	0.745	7.286	7	6.921	23.27	213	-	R
041908+1731.5	20146	8.9100	-	8.6044	0.721	7.134	6.872	6.787	21.55	223	P = new	PE
042013+1914.0	20237	5.4700	5.45	7.5755	0.56	6.395	6.184	6.124	23.19	250	P = P_{lit}	R
042325+1545.8	20485	-	12.38	10.5881	1.231	8.193	7.647	7.494	21.26	213	-	D
042332+1440.2	20492	10.0400	-	9.2505	0.855	7.611	7.255	7.145	21.53	214	P = new	PE
042351+0912.3	-	-	5.33	13.1	1.51	9.117	8.481	8.226	-	189	-	D
042354+1403.1	20527	5.1200	-	11.0037	1.288	8.506	7.925	7.786	21.22	213	P = new	PE
042359+1643.3	-	-	17.14	12.8	1.49	9.421	8.787	8.561	-	226	-	D
042412+1445.5	20553	6.2100	7.1	7.7132	0.604	6.357	6.105	6.007	22.77	212	P = P_{lit}	R
042415+2144.2	20557	31.7000	-	7.2415	0.518	6.148	5.946	5.871	22.59	187	P = new	PE
042417+1800.2	20563	11.4600	11.6	10.1364	1.05	8.154	7.636	7.524	19.31	244	P = P_{lit}	D
042428+1653.2	20577	7.8100	8.05	7.9233	0.599	6.655	6.397	6.29	20.81	228	P = P_{lit}	R
042500+1659.1	-	-	11.77	10.4	1.03	8.486	7.98	7.83	-	226	-	D
042514+1858.4	-	-	10.84	12.8	1.48	9.594	8.958	8.706	-	266	-	D
042548+1801.0	20679	-	8.46	9.1564	0.935	7.314	6.901	6.767	20.79	259	-	D
042606+1531.5	-	5.0100	5.13	7.478	0.543	6.456	6.21	6.14	-	219	P = P_{lit}	R
042625+1651.2	20719	8.0200	7.73	8.1652	0.651	6.841	6.556	6.436	22.21	255	P = P_{lit}	R
042640+1644.8	20741	8.6600	8.67	8.2399	0.664	6.893	6.643	6.547	21.73	259	P = P_{lit}	R
042643+1241.2	20745	-	12.61	10.5767	1.358	7.824	7.209	7.03	29.09	249	-	D
042648+1052.3	20751	-	10.4	9.5825	1.033	7.528	6.968	6.882	24.11	287	-	D

Table 1 – continued from previous page

ASAS ID	HIP ID	P (d)	P$_{lit}$ (d)	V (mag)	B-V (mag)	J (mag)	H (mag)	K (mag)	plx (mas)	LC Pts	note	Ref.
042725+1415.6	-	12.7700	12.776	10.3	1.08	8.374	7.822	7.713	-	266	P = P$_{lit}$	D
042737+1535.2	20815	-	5.87	7.5281	0.537	6.375	6.174	6.141	21.27	266	-	R
042746+1144.2	20826	5.1300	-	7.6166	0.56	6.424	6.222	6.158	21.53	301	P = new	PE
042747+1425.0	20827	10.0900	9.7	9.6272	0.929	7.894	7.456	7.348	19	266	P = P$_{lit}$	D
042804+1352.0	20850	6.2000	-	9.1735	0.839	7.506	7.142	7.003	21.86	277	P = new	PE
042848+1717.1	20899	-	7.41	7.9584	0.609	6.696	6.462	6.404	21.51	309	-	R
042850+1617.5	-	-	3.66	10.73	1.357	8.114	7.555	7.349	-	303	-	R
042931+1614.7	-	-	11.92	10.327	1.167	8.224	7.689	7.515	-	283	-	R
042932+1753.6	20951	9.5800	11.38	9.0821	0.831	7.524	7.149	7.055	23.86	320	P ≠ P$_{lit}$	R
043034+1444.9	-	-	18.41	-	1.56	10.563	9.954	9.712	-	21	-	D
043153+1530.3	21138	-	13.13	11.14	1.28	8.667	8.034	7.895	19.12	250	-	D
043226+1306.8	21179	1.4800	1.48	11.0795	1.194	8.423	7.791	7.654	17.75	260	P = P$_{lit}$	D
043250+1600.4	-	9.2800	9.36	8.933	0.883	7.285	6.859	6.77	-	272	P = P$_{lit}$	R
043259+1549.1	-	-	9.04	8.655	0.741	7.323	7.017	6.941	-	286	-	R
043324+2359.4	-	-	17.55	-	1.52	8.914	8.242	8.028	-	310	-	D
043327+1302.7	-	-	16.29	13.4	1.57	9.683	9.069	8.822	-	204	-	D
043337+2109.1	21256	13.1100	12.69	10.7994	1.237	8.427	7.835	7.686	26.74	303	P = P$_{lit}$	D
043342+1900.9	21261	12.6100	-	10.823	1.197	8.535	7.977	7.82	20.89	379	P = new	PE
043411+1133.5	-	11.5200	11.03	11.3	1.39	8.89	8.3	8.059	-	293	P = P$_{lit}$	D
043435+1530.3	21317	8.7200	8.55	8.0386	0.631	6.745	6.552	6.445	22	247	P = P$_{lit}$	R
043517+2302.7	21380	7.3800	-	9.0505	0.77	7.502	7.171	7.078	20.97	261	P = new	C
043548+1317.1	-	-	13.36	14.9	1.63	10.731	10.108	9.867	-	15	-	D
043605+1541.0	-	-	9.47	9.3	0.87	7.86	7.505	7.373	-	202	-	D
043732+1508.8	21543	6.2100	6.46	7.6601	0.597	6.365	6.099	5.992	20	185	P = P$_{lit}$	R
043951+1243.7	21723	11.2800	10.85	10.1569	1.073	8.089	7.602	7.48	23.33	201	P = P$_{lit}$	D
044006+2318.3	21741	5.9400	-	9.5438	0.811	7.996	7.631	7.565	15.95	216	P = new	PE
044128+1404.6	-	-	1.28	13.3	-	9.576	8.938	8.712	-	167	-	D
044129+1200.6	-	-	18	13	1.5	9.613	8.981	8.754	-	223	-	D
044130+1313.3	-	-	15.42	11.2	1.44	8.356	7.674	7.507	-	184	-	D
044143+0826.2	-	-	8.02	14.7	-	11.979	11.382	11.074	-	5	-	D
044252+1843.2	21923	29.3200	-	7.2549	0.677	5.895	5.578	5.56	22.99	286	P = new	PE
044619+0338.2	22177	-	13.25	11.0224	1.277	8.57	7.984	7.826	23.05	270	-	D

Continued on next page

Table 1 – continued from previous page

ASAS ID	HIP ID	P (d)	P$_{lit}$ (d)	V (mag)	B-V (mag)	J (mag)	H (mag)	K (mag)	plx (mas)	LC Pts	note	Ref.
044630+1528.3	22203	7.7600	7.95	8.439	0.665	7.098	6.843	6.738	21.08	201	P = P$_{lit}$	D
044719+0627.2	-	8.3900	14.44	12	1.42	8.651	8.025	7.875	-	267	P = $\frac{1}{2}$P$_{lit}$	D
044830+1623.3	-	-	15.69	12.6	1.47	9.415	8.773	8.543	-	233	-	D
044842+2106.1	22350	9.6500	9.69	9.2008	0.843	7.522	7.153	7.072	19.41	220	P = P$_{lit}$	D
044904+1838.5	22380	9.5700	-	9.1192	0.833	7.486	7.141	7.059	22.28	286	P = new	PE
044952+0606.5	-	-	17.12	14.5	1.63	10.461	9.886	9.627	-	12	-	D
045001+1624.7	-	-	11.98	10.7	1.16	8.485	7.968	7.839	-	234	-	D
045103+1458.2	-	-	13.14	11.9	-	8.796	8.145	7.967	-	191	-	D
045224+1043.2	-	-	11.34	10.3	1.07	9.633	8.973	8.772	-	289	-	D
045225+1859.9	22654	-	9.88	10.4051	1.07	8.375	7.885	7.742	21.55	353	-	D
045706+2445.1	23027	7.3700	-	8.7438	0.714	7.288	6.986	6.876	21.43	184	P = new	C
050308+1343.8	23498	8.9800	-	9.1222	0.765	7.629	7.303	7.226	17.37	340	P = new	PE
050540+0627.9	23701	9.9800	10.41	10.0026	0.947	8.127	7.631	7.518	19.24	327	P = P$_{lit}$	D
050618+1749.0	23750	7.9000	-	8.945	0.73	7.514	7.216	7.128	19.8	408	P = new	PE
051110+1549.0	-	-	14.94	12.3	-	-	-	-	-	367	-	D
051119+0754.5	-	-	13.23	11.2	-	8.997	8.409	8.301	-	264	-	D
051253+1943.3	24301	14.4300	-	9.9516	1.064	7.761	7.205	7.065	28.62	255	P = new	C

Table 2:: Period distribution for binary stars in the Hyades. P indicates our period measurement. If applicable, P_{lit} is the period determined by the literature source in the reference column. LC PTS refers to the number of datapoints within the ASAS light curve for that star. The note column indicates whether our determined period matches the literature, or whether our period is newly determined from the Perryman et al. catalog or cone search. References - R: Radick et al. (1987), D: Delorme et al. (2011), PE: Perryman et al. (1998), C: our cone search as described in Section 3.

ASAS ID	HIP ID	P (d)	P_{lit} (d)	V (mag)	B-V (mag)	J (mag)	H (mag)	K (mag)	plx (mas)	LC Pts	note	Ref.
033735+2120.6	16908	-	10.57	9.496	0.917	7.645	7.274	7.121	25.18	210	-	D
033934+1823.1	17076	7.2900	-	8.3872	0.81	6.645	6.238	6.179	25.61	275	P = new	C
040039+2022.8	18719	11.1800	-	8.7931	0.705	7.331	7.029	6.912	16.09	410	P = new	PE
041156+2338.2	19591	2.3100	-	9.5365	1.09	7.148	6.563	6.409	26.22	198	P = new	PE
041542+2049.2	19870	9.3200	-	7.9682	0.705	6.537	6.257	6.19	19.23	186	P = new	PE
041739+1656.9	20019	5.5100	-	8.4635	0.756	6.865	6.486	6.397	21.84	222	P = new	PE
042323+1939.5	20482	9.9400	9.9	9.5452	0.908	7.722	7.281	7.151	16.5	213	P = P_{lit}	D
042552+1851.8	20686	7.9400	-	7.6627	0.68	6.269	5.976	5.893	22.58	299	P = new	PE
042829+1741.7	-	-	2.42	12.1	1.49	8.592	7.956	7.711	-	310	-	D
042837+1944.4	20890	11.5600	11.52	8.755	0.741	7.292	6.996	6.908	21.15	301	P = P_{lit}	R
043035+1544.0	-	-	8.73	8.8	0.84	7.336	6.902	6.817	-	230	-	D
043359+1509.8	21280	8.7300	-	8.6372	0.84	6.989	6.576	6.465	23.95	260	P = new	PE
044316+1704.1	-	10.1600	10.31	9.9	1	8.002	7.528	7.396	-	234	P = P_{lit}	D
044649+1744.9	22224	10.3000	-	9.7398	0.967	7.798	7.298	7.171	24.09	231	P = new	PE
044801+1703.4	-	-	10.77	11.7	1.41	8.214	7.592	7.374	-	233	-	D
044913+2448.1	22394	7.0500	6.9	9.6468	1.052	7.582	7.12	6.956	20.11	185	P = P_{lit}	D
045034+1505.0	22505	8.7300	-	7.8651	0.74	6.439	6.133	6.044	23.69	190	P = new	PE

5.1. Error Analysis

We were able to measure periods for 27 stars with previously determined periods. A comparison of our calculated period and the literature period is shown in Fig. 13.

We find that there are two stars that lie near alias lines: 044719+0627.2 is measured at half of the value of the literature period, and 040811+1652.4 has a measured period that is roughly 2.5 times greater than the literature value.

Looking at the other 25 points on the plot, we find that the standard deviation of the difference between our value and the literature value is 0.5 days. We ascribe a 2σ uncertainty of 1 day to our period determination for each star.

6. Gyrochronology

Observations of open clusters have shown that there are two main timescales at which stars spin down as a result of interior dynamo mechanics. Stars begin on the main sequence as fast rotating, convective C-type stars with a de-coupled radiative and convective zone. The outer convective layer of C-type stars spin down at an exponential rate (Barnes 2003). Over time, the radiative and convective zones become coupled and a star begins rotating at as a solid body. Solid body rotators follow the Skumanich spin-down relation where rotational velocity is proportional to $t^{-0.5}$ (Skumanich 1972). These stars are known as interface I-type stars and are rotating slower than the C-type stars, occupying a distinct sequence on a mass-period plot for a given cluster. The number of stars that have transitioned from the C-sequence to the I-sequence in a cluster increases over time. At the age of the Hyades, the majority of stars are found along the I-sequence.

6.1. Empirically derived color-period relation

Barnes (2003) empirically determined the relationship between rotation, color, and age for I-sequence stars to be to be a separable function of stellar mass (as given by stellar color, an observable proxy) and age:

$$P = f(B - V) \cdot g(t). \tag{18}$$

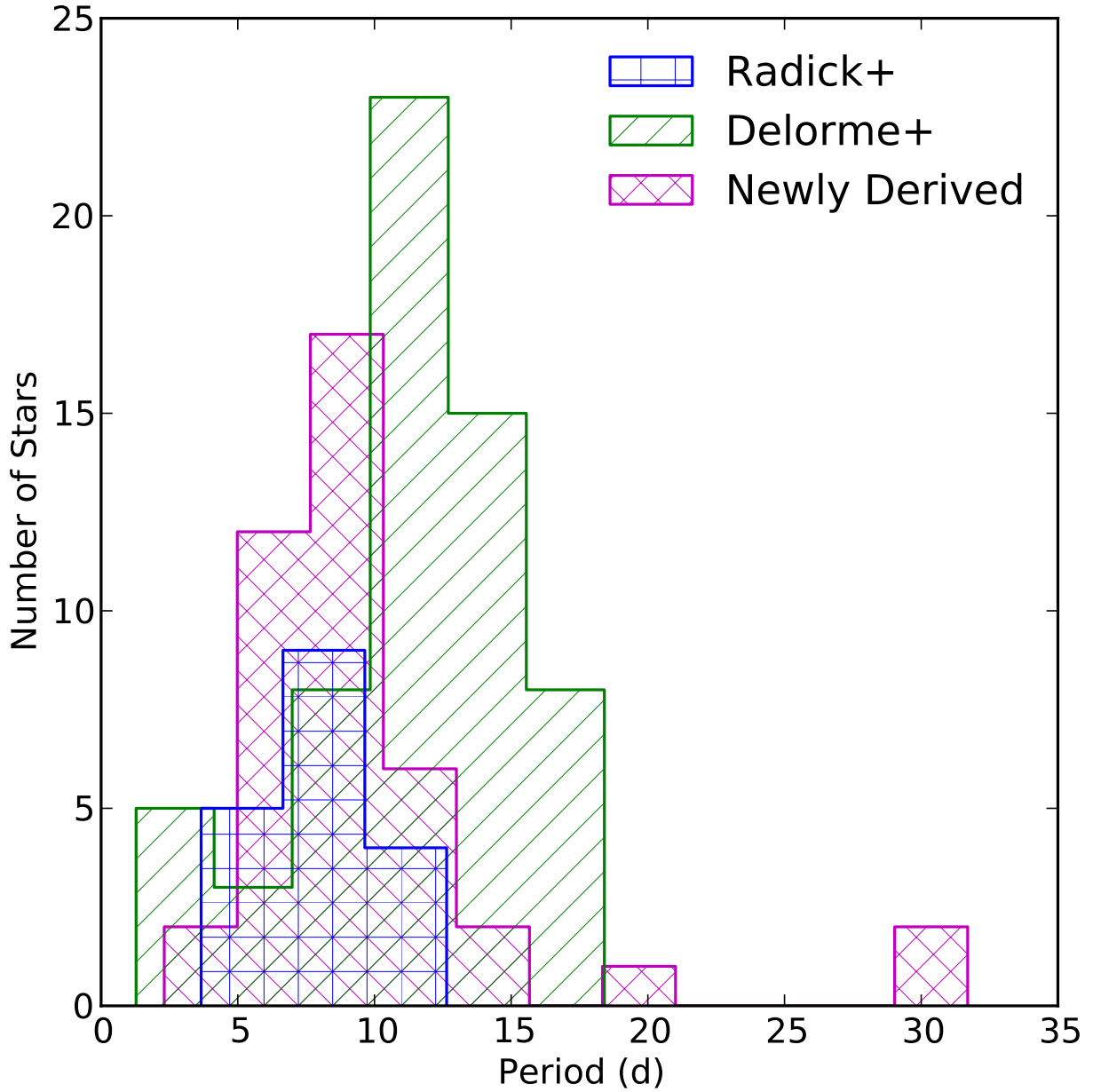Based on rotation period studies of multiple open clusters, Barnes (2007) determined:

Fig. 11.— The period distrubution for Hyads with rotation periods. The literature periods have been used to create the Radick+ and Delorme+ distributions. The newly derived distribution contains only those periods who have been determined for the first time as a result of this study.
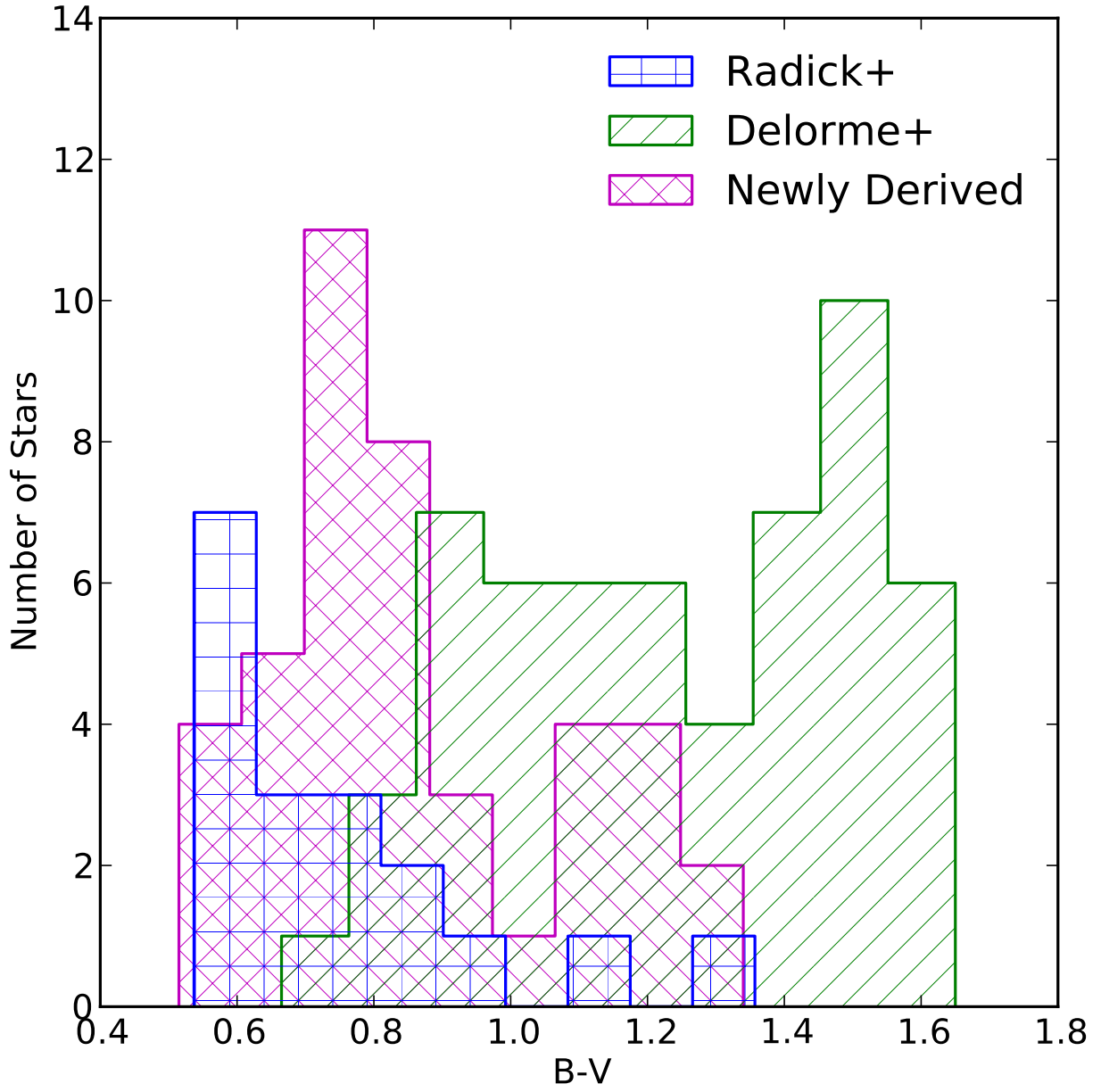
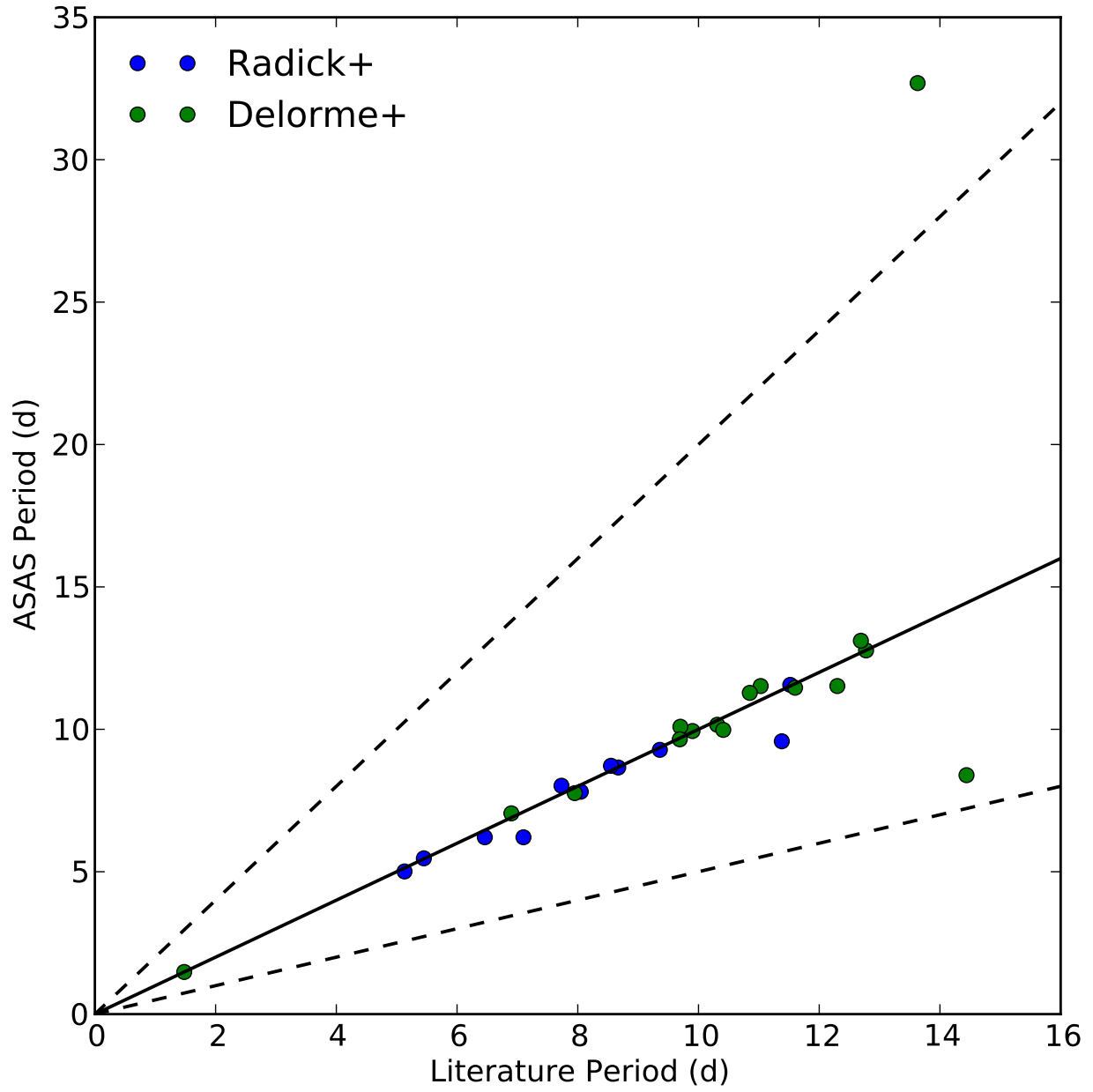Fig. 12.— The B-V distribution of Hyads with rotation periods.

Fig. 13.— A comparison of our determined ASAS period and the period published in previous studies. The dashed lines indicate half and double the literature period values.

$$f(B-V) = a(B-V-c)^b \tag{19}$$

and

$$g(t) = t^n. \tag{20}$$

Over a range of solar-type B-V values, Eq. 18 traces out the I-sequence for a cluster of a given age. The coefficients a, b, c, and n control the overall shape and position of the age-parameterization curve in color-period space. In order to determine the coefficients in Eq. 18, Barnes (2007) used a large collection of open clusters spanning from 30 - 600 Myr and the solar datum to calibrate the mass proxy, $f(B-V)$, and age dependence, $g(t)$, respectively. An alternative calibration was performed by Mamajek and Hillenbrand (2008) using a different dataset consisting of a few benchmark open clusters and the solar datum. The authors claimed that this calibration better represented the mass and age dependence of their dataset compared to Barnes (2007). More recently, Meibom et al. (2009) used a large sample ($\sim$300) of rotation periods in the 135 Myr open cluster M35 to derive an additional set of gyrochrone parameters. This is currently one of the largest rotation period datasets for any single open cluster in this age range (> 100 Myr). A summary of the empirical parameter calibrations is shown in Table 6.1. Using an age of 625 Myr for the Hyades based on a previous isochrone fitting age determination (Perryman et al. 1998), we plot the predicted gyrochrones for each empirical calibration in Fig. 14.

We find that for the high mass stars (B-V < 0.8), the three gyrochrones are indistinguishable from each other with a 1 day error on the stellar rotation periods. For the range $0.8 <$ B-V < 1.6, all three gyrochrones predict slower rotation periods at 625 Myr than what is observed. The form of the Mamajek & Hillenbrand curve appears to follow the shape of the observed Hyades I-sequence; however, an age of ~ 500 Myr would be required for this relationship to accurately reproduce the late-type Hyades rotation sequence. At a B-V of $\sim$1.6 stars have effectively become fully convective. As a result, the spindown timescale may not follow the Skumanich-like spindown of I-sequence stars and the gyrochrones are not expected to accurately model the observed rotation periods.

Parameter	Barnes 07	M&H 08	Meibom+ 09
a	0.7725 ± 0.011	0.407 ± 0.021	0.77 ± 0.014
b	0.601 ± 0.024	0.325 ± 0.024	0.553 ± 0.052
c	0.4	0.495 ± 0.010	0.472 ± 0.027
n	0.5189 ± 0.007	0.566 ± 0.008	0.52

Table 3: The values for each parameter used in Eq. 18 as calculated by three previous studies.
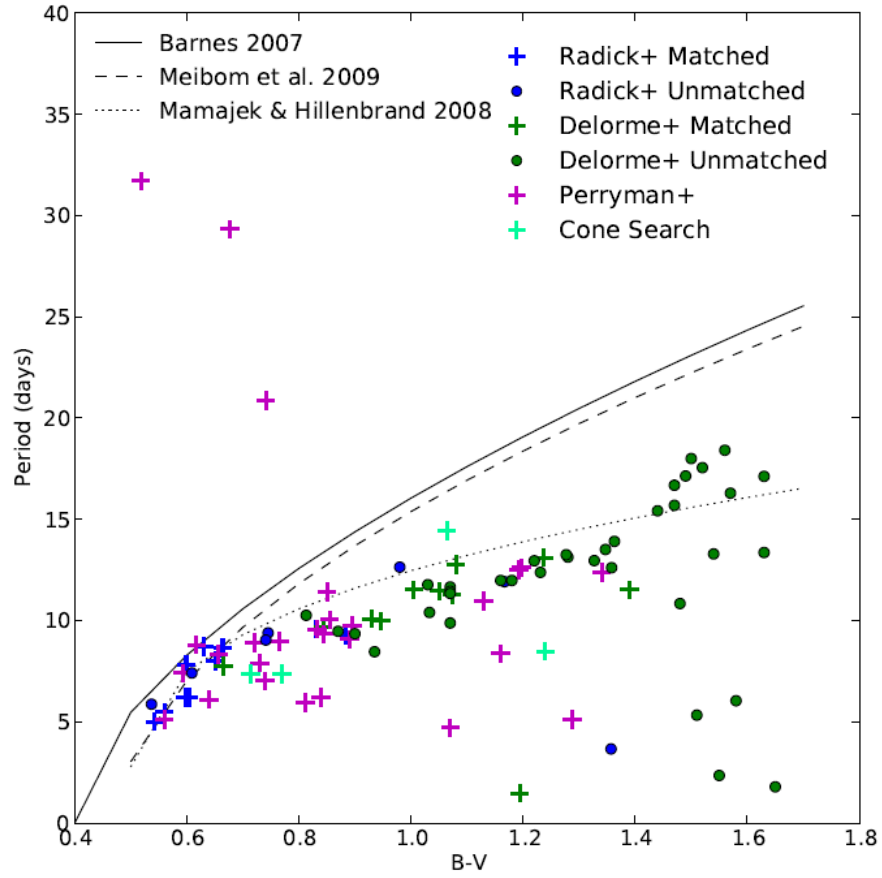
Fig. 14.— The color-period distribution for the single star Hyades cluster members (Table 1) with overplotted empirically derived gyrochrones from three open cluster studies.

6.2. Theory based τ - period relation

Barnes and Kim (2010) derived equations of the rate loss of angular momentum for I-sequence and C-sequence stars based on observational data of open clusters. The rate loss equations are dependent upon the spin-down timescales of both sequences which were shown to be a function of the convective turnover timescale τ. τ is related to the depth of the convective zone of a star which is fundamentally related to the mass and color of a star.

Using the Barnes & Kim relation of stellar spindown and τ, Barnes (2010) determined a non-linear model relating τ, rotation period P, and stellar age t:

$$\tau = \frac{k_C t \pm \sqrt{(k_C t)^2 2 k_I k_C P_0^2 (x^2 - 1) \ln(\frac{P}{P_0})}}{2 \ln(\frac{P}{P_0})}. \tag{21}$$

.

The initial period P_0 is the rotation period a star has when it reaches the zero-age main sequence. k_C and k_I are constants required to transform the C-sequence and I-sequence spin-down timescales into a function of the convective turnover timescale. The values of these constants have been approximately determined to be $k_C = 0.646$ days/Myr and $k_I = 452$ Myr/days (Barnes 2010). Barnes & Kim calculated equivalent τ, mass, and color values that we have used to convert the τ - period relation into a mass-period relation.

Fig. 15 shows the mass-period diagram for the 103 single star Hyades members with rotation periods (the entirety of Table 1). 625 Myr gyrochrones calculated from Eq. 21 have been overplotted at initial periods of $P_0 = .12$, 1.1, and 3.4 days.

6.3. Gyrochronology Analysis

Barnes (2010) solves Eq. 21 for the age of a star t:

$$t = \frac{\tau}{k_C} \ln(\frac{P}{P_0}) + \frac{k_I}{2\tau}(P^2 - P_0^2). \tag{22}$$

Barnes (2010) chose $P_0 = 1.1$ days to calibrate his model to the sun's current observed rotation, age, and mass. As a result, $P_0 = 1.1$ d is an appropriate choice for solar-mass stars. Determining the initial rotation period of a star otherwise is nearly impossible. Calculating ages for individual cluster members using Eq. 22 and $P_0 = 1.1$ d creates the age distribution shown in Fig. 16. The spread of ages about the mode arises from the spread of initial periods about 1.1 d.
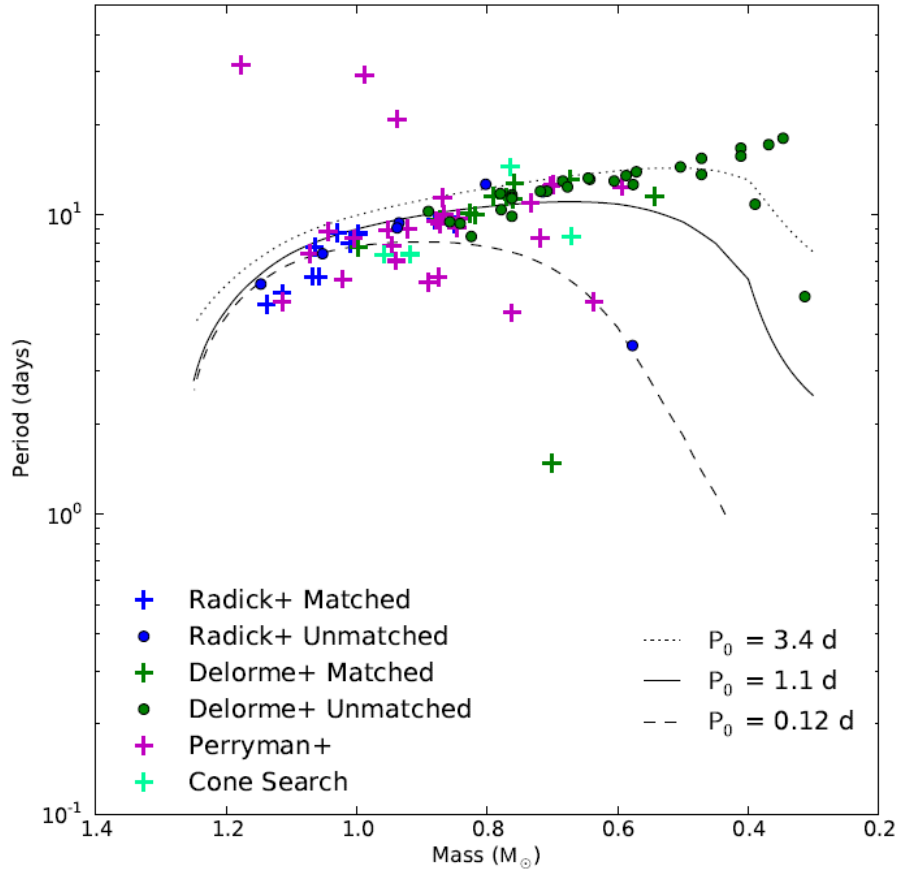
Fig. 15.— Mass-period distribution of the Hyades with over-plotted 625 Myr gyrochrones. Each line corresponds to the predicted rotation rate at a given mass and with the same initial rotation period P_0 at this age.

In order to investigate any mass dependent characterisitics of the distribution of calculated ages, the distribution was divided into three mass bins shown in Fig. 17. The range of each mass bin was determined based on where the observed I-sequence transitions between gyrochrones of different P_0 as seen in Fig. 15. The majority of stars of a mass $M > M_\odot$ were modeled best assuming $P_0 = .12$ d, stars in the range $0.7M_\odot < M < 1M_\odot$ mostly followed the $P_0 = 1.1$ d gyrochrone, while stars of $M < 0.7M_\odot$ mostly lined up with the $P_0 = 3.4$ d gyrochrone. The spread of the distributions in each mass bin is again related to the spread of P_0 about 1.1 d. As seen in Fig. 15, the high mass stars have almost converged to a single sequence, while the low mass stars have a wide distrubution of rotation periods, a result of high-mass stars reaching convergence earlier than low-mass stars. This is reflected in Fig. 17 where the high mass age distribution has a low σ value compared to the higher σ value for the low mass stars.

It is well known that star formation in open clusters occurs over the span of a few million years e.g., in the 1 Myr Orion Nebula Cluster the age spread is only seen to be 1-5 Myr (Jeffries et al. 2011). We can therefore rule out an age dependence on mass as indicated by the dissimilar modes of each distribution. Another possibility is that differences of the modes indicate a dependence of the calculated age on the choice of P_0. For example, in Fig. 15, the majority of the low mass stars lie on a 625 Myr gyrochrone with $P_0 = 3.4$ d. If we were to instead assume the majority of the low mass stars began with $P_0 = 1.1$ d, as we have in Fig. 17, we would find the low mass stars to lie on a gyrochrone of $t = 736$ Myr as shown in Fig. 18. However, the most probable explanation for the dissimilarity of the modes is that the Barnes (2010) model itself does not take into account the complexity of angular momentum loss for high and low mass stars.
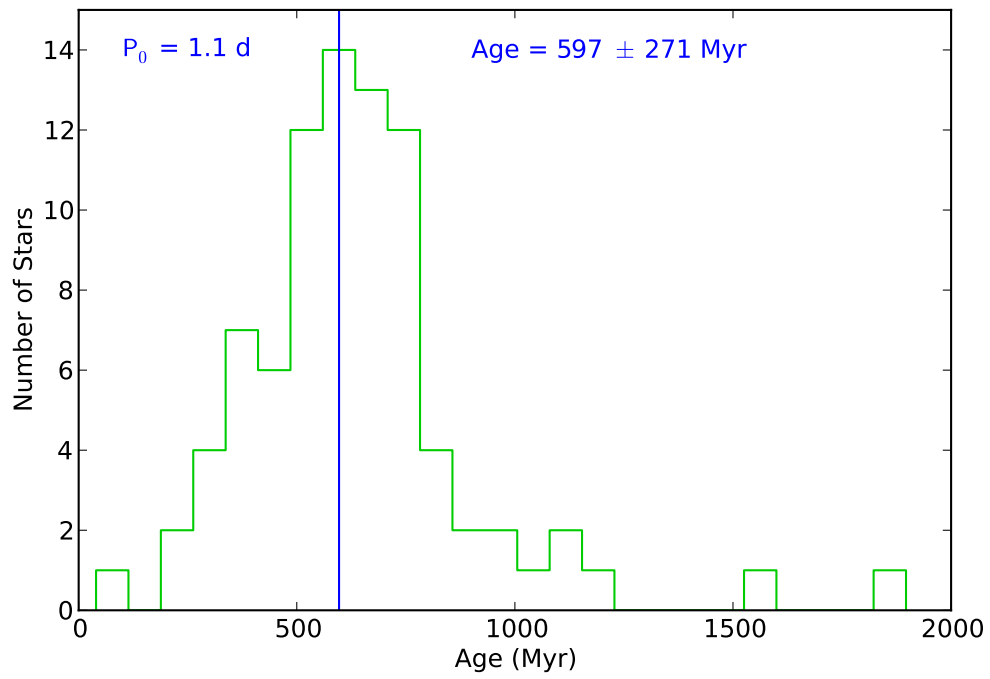
Fig. 16.— Gyro-ages determined for the Hyades based on our dataset of rotation periods. We have assumed an initial rotation period of 1.1 days. The vertical line is the mode of the distribution.
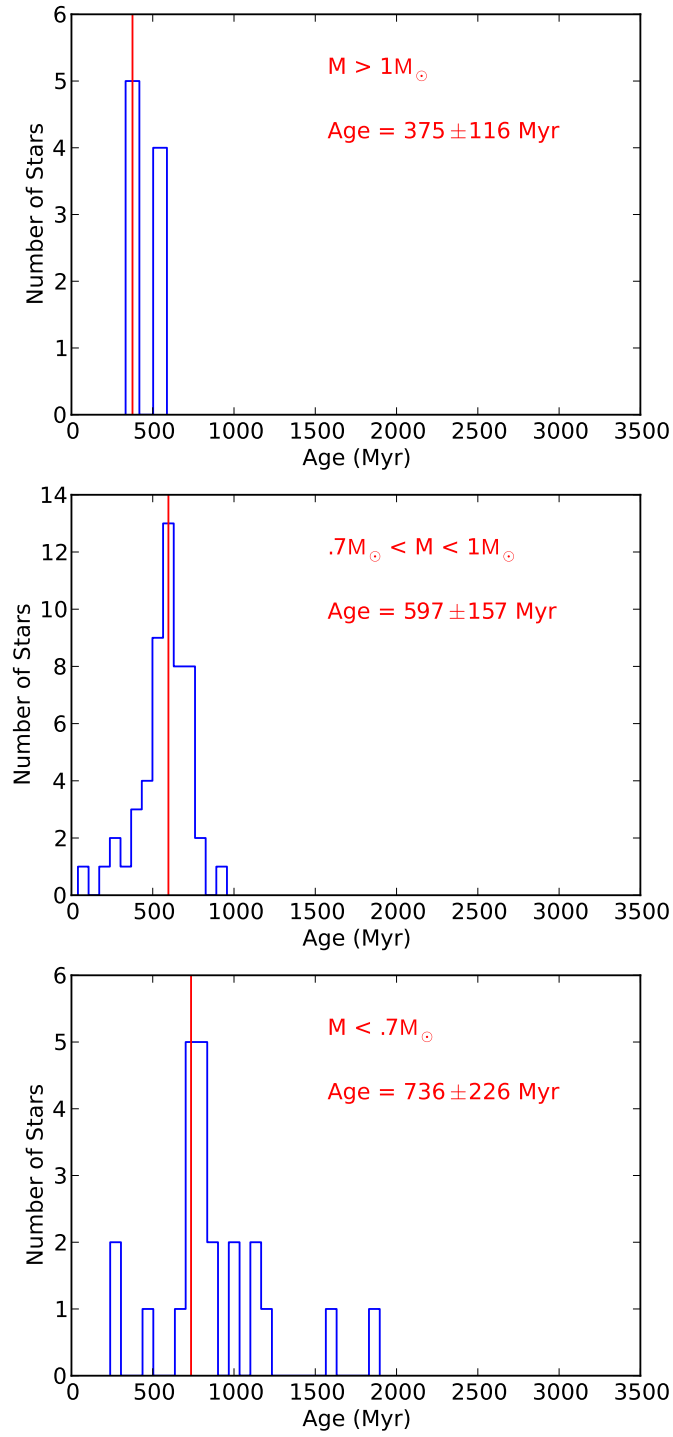
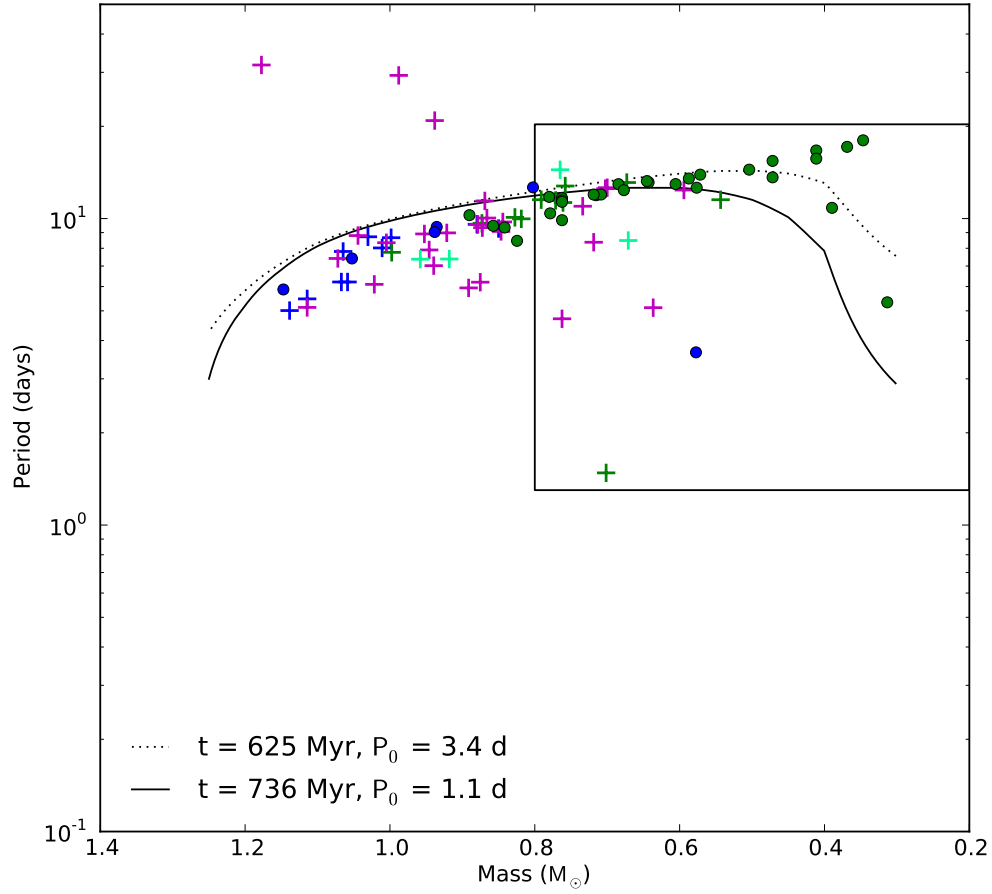Fig. 17.— A separation of Fig. 16 into mass bins.

Fig. 18.— An almost convergence of two gyrochrones of different ages and initial periods.

7. Applications for LSST & Future Work

Our results in Section 5 indicate that determining rotation periods from low cadence, sparsely sampled light curves is possible. We carried out an additional analysis to determine how few data points are needed to determine a reliable rotation period from long duration data.

We performed our light curve analysis on 100 and 200 randomly selected data points from an ASAS light curve and repeated this process 1000 times. A recovery efficiency (REff) was calculated based on the number of rotation periods returned out of 1000. A precision efficiency (PEff) was calculated based on the number of period returns within 1 day of the mode of the distribution out of 1000. An example of this is shown in Fig. 19. As one would expect, the number of returned periods decreases with decreasing number of data points.

We will apply this type of Monte Carlo analysis to a larger sample of ASAS data to get more robust statistics in the future. However, based on our preliminary results, it seems likely that high fidelity rotation periods can be derived from LSST type data by implementing similar techniques to what we have presented in this paper.
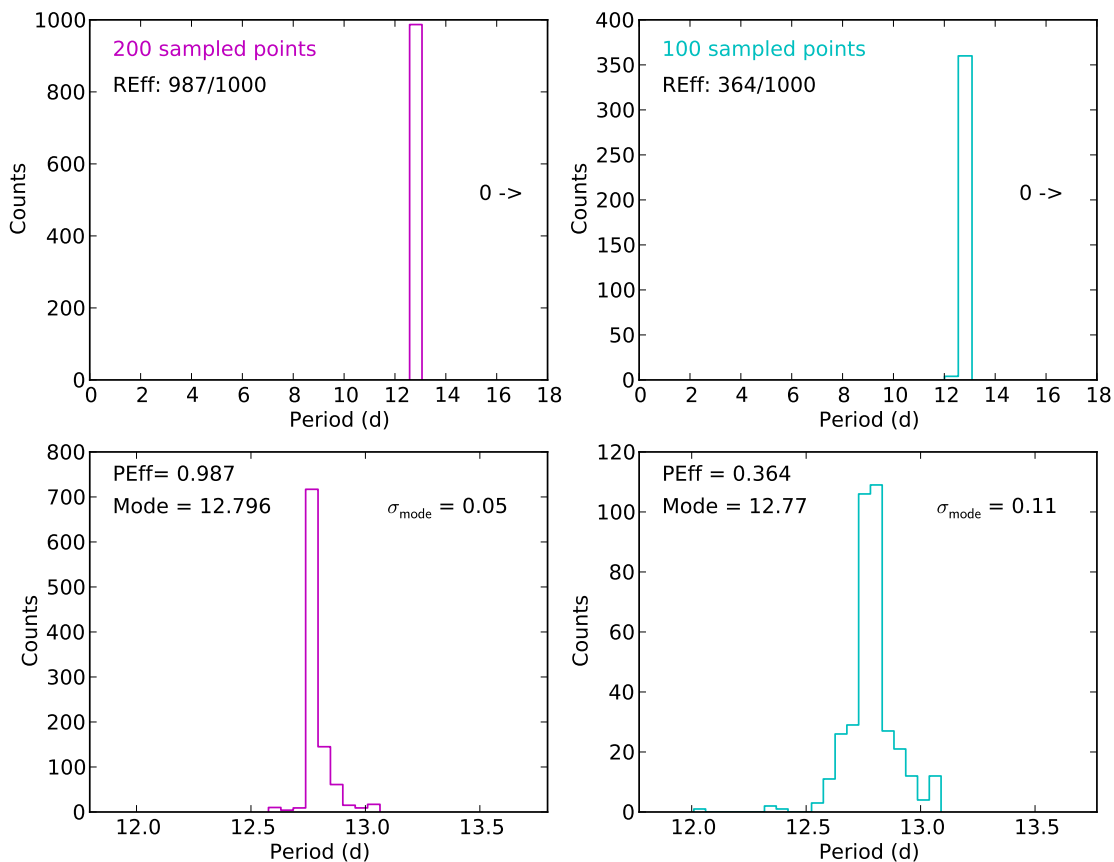
Fig. 19.— The results of performing a Monte Carlo subsampling of the ASAS 042725+1415.6 light curve. We note that every returned period fell within 1 day of the mode of the distribution. Additionally, when we only used a FAP < 0.05 as a requirement for reliability, the precision efficiency was ∼ 0.7.

REFERENCES

S. A. Barnes. On the Rotational Evolution of Solar- and Late-Type Stars, Its Magnetic Origins, and the Possibility of Stellar Gyrochronology. ApJ, 586:464–479, March 2003. doi: 10.1086/367639.

S. A. Barnes. Ages for Illustrative Field Stars Using Gyrochronology: Viability, Limitations, and Errors. ApJ, 669:1167–1189, November 2007. doi: 10.1086/519295.

S. A. Barnes. A Simple Nonlinear Model for the Rotation of Main-sequence Cool Stars. I. Introduction, Implications for Gyrochronology, and Color-Period Diagrams. ApJ, 722:222–234, October 2010. doi: 10.1088/0004-637X/722/1/222.

S. A. Barnes and Y.-C. Kim. Angular Momentum Loss from Cool Stars: An Empirical Expression and Connection to Stellar Activity. ApJ, 721:675, September 2010. doi: 10.1088/0004-637X/721/1/675.

J. H. J. de Bruijne, R. Hoogerwerf, and P. T. de Zeeuw. A Hipparcos study of the Hyades open cluster. Improved colour-absolute magnitude and Hertzsprung-Russell diagrams. A&A, 367:111–147, February 2001. doi: 10.1051/0004-6361:20000410.

P. Delorme, A. Collier Cameron, L. Hebb, J. Rostron, T. A. Lister, A. J. Norton, D. Pollacco, and R. G. West. Stellar rotation in the Hyades and Praesepe: gyrochronology and braking time-scale. MNRAS, 413:2218–2234, May 2011. doi: 10.1111/j.1365-2966.2011.18299.x.

W. Herbst, C. A. L. Bailer-Jones, R. Mundt, K. Meisenheimer, and R. Wackermann. Stellar rotation and variability in the Orion Nebula Cluster. A&A, 396:513–532, December 2002. doi: 10.1051/0004-6361:20021362.

J. H. Horne and S. L. Baliunas. A prescription for period analysis of unevenly sampled time series. ApJ, 302:757–763, March 1986. doi: 10.1086/164037.

R. D. Jeffries, S. P. Littlefair, T. Naylor, and N. J. Mayne. No wide spread of stellar ages in the Orion Nebula Cluster. MNRAS, 418:1948–1958, December 2011. doi: 10.1111/j.1365-2966.2011.19613.x.

S. D. Kawaler. Angular momentum loss in low-mass stars. ApJ, 333:236–247, October 1988. doi: 10.1086/166740.

LSST Science Collaborations, P. A. Abell, J. Allison, S. F. Anderson, J. R. Andrew, J. R. P. Angel, L. Armus, D. Arnett, S. J. Asztalos, T. S. Axelrod, and et al. LSST Science Book, Version 2.0. *ArXiv e-prints*, December 2009.

E. E. Mamajek and L. A. Hillenbrand. Improved Age Estimation for Solar-Type Dwarfs Using Activity-Rotation Diagnostics. ApJ, 687:1264–1293, November 2008. doi: 10.1086/591785.

S. Meibom, R. D. Mathieu, and K. G. Stassun. Stellar Rotation in M35: Mass-Period Relations, Spin-Down Rates, and Gyrochronology. ApJ, 695:679–694, April 2009. doi: 10.1088/0004-637X/695/1/679.

S. Messina, S. Desidera, M. Turatto, A. C. Lanzafame, and E. F. Guinan. RACE-OC Project: Rotation and variability in young stellar associations within 100 pc. *ArXiv e-prints*, April 2010.

L. Mestel and H. C. Spruit. On magnetic braking of late-type stars. MNRAS, 226:57–66, May 1987.

G. Meynet and A. Maeder. Stellar evolution with rotation. I. The computational method and the inhibiting effect of the μ-gradient. A&A, 321:465–476, May 1997.

E. N. Parker. Dynamics of the Interplanetary Gas and Magnetic Fields. ApJ, 128:664, November 1958. doi: 10.1086/146579.

M. A. C. Perryman, A. G. A. Brown, Y. Lebreton, A. Gomez, C. Turon, G. Cayrel de Strobel, J. C. Mermilliod, N. Robichon, J. Kovalevsky, and F. Crifo. The Hyades: distance, structure, dynamics, and age. A&A, 331:81–120, March 1998.

G. Pojmanski. The All Sky Automated Survey. Catalog of Variable Stars. I. 0 h - 6 hQuarter of the Southern Hemisphere. Acta Astron., 52:397–427, December 2002.

W. H. Press and G. B. Rybicki. Fast algorithm for spectral analysis of unevenly sampled data. ApJ, 338:277–280, March 1989. doi: 10.1086/167197.

R. R. Radick, D. T. Thompson, G. W. Lockwood, D. K. Duncan, and W. E. Baggett. The activity, variability, and rotation of lower main-sequence Hyades stars. ApJ, 321: 459–472, October 1987. doi: 10.1086/165645.

D. H. Roberts, J. Lehar, and J. W. Dreher. Time Series Analysis with Clean - Part One - Derivation of a Spectrum. AJ, 93:968, April 1987. doi: 10.1086/114383.

J. D. Scargle. Studies in astronomical time series analysis. II - Statistical aspects of spectral analysis of unevenly spaced data. ApJ, 263:835–853, December 1982. doi: 10.1086/160554.

E. Schatzman. A theory of the role of magnetic activity during star formation. *Annales d'Astrophysique*, 25:18, February 1962.

A. Skumanich. Time Scales for CA II Emission Decay, Rotational Braking, and Lithium Depletion. ApJ, 171:565, February 1972. doi: 10.1086/151310.

P. A. Sturrock. Solar Neutrino Variability and Its Implications for Solar Physics and Neutrino Physics. ApJ, 688:L53–L56, November 2008. doi: 10.1086/594993.

P. A. Sturrock and J. D. Scargle. False-alarm Probability in Relation to Oversampled Power Spectra, with Application to Super-Kamiokande Solar Neutrino Data. ApJ, 718: 527–529, July 2010. doi: 10.1088/0004-637X/718/1/527.

P. A. Sturrock, J. D. Scargle, G. Walther, and M. S. Wheatland. Combined and Comparative Analysis of Power Spectra. Sol. Phys., 227:137–153, March 2005. doi: 10.1007/s11207-005-7424-x.

F. van Leeuwen. Validation of the new Hipparcos reduction. A&A, 474:653–664, November 2007. doi: 10.1051/0004-6361:20078357.

F. van Leeuwen. Parallaxes and proper motions for 20 open clusters as based on the new Hipparcos catalogue. A&A, 497:209–242, April 2009. doi: 10.1051/0004-6361/200811382.

E. J. Weber and L. Davis, Jr. The Angular Momentum of the Solar Wind. ApJ, 148:217–227, April 1967. doi: 10.1086/149138.